



HAL
open science

Magnetic boundary layers in numerical dynamos with heterogeneous outer boundary heat flux

Filipe Terra-Nova, Hagay Amit

► **To cite this version:**

Filipe Terra-Nova, Hagay Amit. Magnetic boundary layers in numerical dynamos with heterogeneous outer boundary heat flux. *Physics of the Earth and Planetary Interiors*, 2020, 309, pp.106589. 10.1016/j.pepi.2020.106589 . hal-03027314

HAL Id: hal-03027314

<https://hal.science/hal-03027314>

Submitted on 19 Nov 2021

HAL is a multi-disciplinary open access archive for the deposit and dissemination of scientific research documents, whether they are published or not. The documents may come from teaching and research institutions in France or abroad, or from public or private research centers.

L'archive ouverte pluridisciplinaire **HAL**, est destinée au dépôt et à la diffusion de documents scientifiques de niveau recherche, publiés ou non, émanant des établissements d'enseignement et de recherche français ou étrangers, des laboratoires publics ou privés.

Magnetic boundary layers in numerical dynamos with heterogeneous outer boundary heat flux

Filipe Terra-Nova^{a,*}, Hagay Amit^b

^a Departamento de Geofísica, Instituto de Astronomia, Geofísica e Ciências Atmosféricas, Universidade de São Paulo, Rua do Matão, 1226, Cidade Universitária, 05508-090 São Paulo, Brazil

^b CNRS, Université de Nantes, Nantes Atlantiques Universités, UMR CNRS 6112, Laboratoire de Planétologie et de Géodynamique, 2 rue de la Houssinière, F-44000 Nantes, France

ABSTRACT

It has been proposed that magnetic flux expulsion due to outer core fluid upwellings may affect the geomagnetic secular variation on the core-mantle boundary (Bloxham, 1986). In this process intense horizontal field lines are concentrated below the outer boundary, introducing small radial length scales and consequently strong radial diffusion. Here we explore such magnetic boundary layers in numerical dynamo simulations with heterogeneous outer boundary heat flux inferred from a tomographic model of lower mantle seismic shear waves velocity anomalies. Our scheme associates magnetic boundary layers to peak horizontal magnetic fields at the top of the shell. In our models mean magnetic boundary layer thickness ranges $\approx 200 - 400$ km and decreases with increasing magnetic Reynolds number. Extrapolation or interpolation to Earth's core conditions based on total core flow amplitude or its poloidal part gives mean magnetic boundary layer thickness of ≈ 220 and $\approx 260 - 330$ km, respectively. We find magnetic boundary layers associated with the azimuthal field at the equatorial region, whereas magnetic boundary layers associated with the meridional field are found at mid latitudes. Negative outer boundary heat flux anomalies yield preferred locations of expulsion of azimuthal field below Africa and the Pacific, while positive outer boundary heat flux anomalies yield preferred locations of expulsion of meridional field below the Americas and East Asia. Furthermore, we find a tendency of the azimuthal field to low latitudes of the Northern Hemisphere. Our results suggest that the local diffusion time is on the order of several kyr and the local magnetic Reynolds number is on the order of ≈ 10 , both much smaller than classical estimates.

1. Introduction

Boundary layers are fundamental features of fluid systems. In no-slip conditions a viscous layer reduces a finite amplitude flow at the bulk to zero on the boundary. When rotation effects dominate the dynamics, the flow in an Ekman layer not only decreases in magnitude but also spirals, leading e.g. to a non-trivial angle between the atmospheric wind and the vertically integrated flow at the top of the ocean (e.g. Pedlosky, 1987). In a system that cools, a thermal boundary layer with cold fluid is formed below the upper boundary (as in the lithosphere); this dense cold material sinks, as in subducting plates (e.g. Schubert et al., 2001). In the presence of a magnetic field component perpendicular to the boundary, a Hartmann layer provides a path for electrical currents (e.g. Alboussière and Lingwood, 2000). Boundary layers may affect and even determine the fluid dynamics at depth. For example, competing effects of Ekman and thermal boundary layers may determine the dynamics in a plane layer rotating Rayleigh-Bénard convection (King et al., 2009). Likewise, in simulations of convection in a rotating spherical shell, boundary layer effects also control the transition between rotation-dominated and buoyancy-dominated regimes (Gastine et al., 2016; Long et al., 2020).

Convection in Earth's metallic outer core may form magnetic boundary layers. Based on geomagnetic observations, conflicting arguments were put forward against (Whaler, 1980; Lloyd and Gubbins, 1990) vs. in favor (Whaler, 1986; Beggan and Whaler, 2008; Amit, 2014; Lesur et al., 2015; Hugué et al., 2018) of fluid upwelling and downwelling below the core-mantle boundary (CMB), the latter even in the presence of a stratified layer (Buffett, 2014; Buffett et al., 2016; Olson et al., 2018). Bloxham (1986) studied the effects of steady upwelling on an initial toroidal magnetic field in a 2D framework. He showed that upwelling bends and advects toroidal field lines towards the top of the container. On approach to the outer boundary the horizontal field lines become dense. Radial diffusion in this location leads to expulsion of a pair of opposite-sign poloidal flux patches on the outer boundary. If the upwelling persists the field lines get denser and the flux patches intensify. From hereafter we therefore define “magnetic boundary layer” as a location in which intense horizontal magnetic field resides at the top of the shell, culminating in flux expulsion to the outer boundary by radial diffusion.

Aubert et al., 2008b confirmed the simplified kinematic model of Bloxham (1986) in self-consistent numerical dynamos. They designed an imaging scheme to study the 3D structure of magnetic field lines

* Corresponding author.

E-mail address: filipeterranova@iag.usp.br (F. Terra-Nova).

inside the shell. Indeed in their models upwellings locally concentrate toroidal field lines at the top of the shell with corresponding pairs of opposite-sign flux patches on the outer boundary.

Recently the magnetic flux expulsion model of [Bloxham \(1986\)](#) was revisited by [Troyano et al. \(2020\)](#). They examined various magnetic boundary conditions and flow patterns. Furthermore, they explored simulations with a far larger range of magnetic Reynolds numbers

$$Rm = UD/\eta, \quad (1)$$

where U is a typical velocity scale, D is a typical length scale and η is the magnetic diffusivity. Focusing on the enigmatic observation of archeomagnetic spikes ([Ben-Yosef et al., 2009](#); [Shaar et al., 2011, 2016](#)), [Troyano et al. \(2020\)](#) developed scaling laws for the maximum magnetic energy of the system and for the maximum radial field on the outer boundary, both as functions of Rm . Applying their scaling laws to Earth's core, they concluded that magnetic flux expulsion cannot explain the observed archeomagnetic spikes.

If applicable to Earth's core, the final step of the model of [Bloxham \(1986\)](#) requires significant radial magnetic diffusion in the geomagnetic secular variation (SV). Observational evidence for geomagnetic diffusion correspond to total unsigned flux inside null-curves (i.e. zero radial field contours) on the CMB that varies with time ([Backus, 1968](#); [Chulliat and Hulot, 2001](#)). [Bloxham and Gubbins \(1985, 1986\)](#) showed that there are regions e.g. under the South Atlantic where the total flux inside null-curves has drastically evolved. [Chulliat and Olsen \(2010\)](#) found similar evidence for radial diffusion below the Atlantic using a higher resolution and reliability field and SV models based on satellite data. However, remaining uncertainty in the precise topology of null-curves in geomagnetic field models casts doubts on such inferences ([Whaler and Holme, 2007](#); [Gillet et al., 2013](#)).

Another evidence for radial magnetic diffusion on the CMB, and hence for the existence of relatively thin magnetic boundary layers at the top of the core, comes from the observed geomagnetic dipole decay. The geomagnetic axial dipole has been decreasing since the field intensity has been measured (e.g. [Gubbins, 1987](#); [Finlay, 2008](#)) and perhaps even before ([Poletti et al., 2018](#)). Although dipole decay can be caused by poleward/equatorward transport of reversed/normal magnetic flux respectively ([Olson and Amit, 2006](#); [Finlay et al., 2016](#)), advection has limited efficiency in producing continuous dipole collapse ([Moffatt, 1978](#)). The geomagnetic dipole decay has been accompanied by the expansion and intensification of reversed flux patches on the CMB ([Gubbins, 1987](#); [Olson and Amit, 2006](#); [Terra-Nova et al., 2015](#); [Finlay et al., 2016](#); [Metman et al., 2018](#)), which provide further evidence for significant magnetic diffusion in the SV.

These inferences from geomagnetic observations may seem in contradiction with the very large estimates of the magnetic Reynolds number at the top of the core. Using the outer core thickness $D = 2265$ km ([Dziewonski and Anderson, 1981](#)) together with classical values for the flow magnitude $U = 5 \cdot 10^{-4}$ m/s and fluid magnetic diffusivity $\eta = 1 \text{ m}^2/\text{s}$ (1) gives $Rm \approx 1000$, which suggests that on large length scales and short timescales diffusion is negligible in the geomagnetic SV. This supports the frozen-flux approximation in core flow inversions ([Roberts and Scott, 1965](#)). However, these estimates of Rm use as length scale the same thickness of the outer core D for both induction and diffusion processes. If thin magnetic boundary layers prevail at the top of the core, then the appropriate length scale for diffusion (given by the thickness of these layers) is much smaller. This suggests that the effective magnetic Reynolds number characterizing the induction at the top of the core may be significantly smaller than commonly assumed ([Finlay and Amit, 2011](#)), at least in some locations.

Despite its inaccessibility in the observations, some attempts were made to account for diffusion in core flow models inferred from geomagnetic SV inversions. [Amit and Christensen \(2008\)](#) found in numerical dynamos that the radial and tangential magnetic diffusion contributions to the SV are correlated. Knowledge of tangential diffusion from field models allows incorporating the full diffusion term in

core flow inversions. They obtained a flow pattern close to that of models that were inverted neglecting diffusion, but with higher amplitudes and some regional differences, e.g. below North America and Asia. [Finlay et al. \(2016\)](#) compared a quasi-geostrophic frozen-flux core flow model ([Gillet et al., 2015b](#)) with a model based on data assimilation of spatial constraints from numerical dynamo models which permits decomposition to advective and diffusive parts ([Aubert, 2013](#); [Aubert et al., 2013](#)). [Finlay et al. \(2016\)](#) found encouraging morphological similarity between the two flow models. Focusing on contributions to the axial dipole SV, they found that advection dominates at most times although diffusion has a larger contribution at some years. [Barrois et al. \(2017, 2018\)](#) used spatial and temporal constraints derived from geodynamo simulations and stochastic differential equations to invert for a core flow using Kalman filter where they account for induction, diffusion and sub-grid effects. Their core flow model contains several features found by previous studies e.g. the eccentric gyre ([Pais and Jault, 2008](#)) but also some equatorial asymmetric features. Recently, [Gillet et al. \(2019\)](#) followed the approach of [Barrois et al. \(2017\)](#) but relied on the spatial and temporal statistics from the 'Mid-Path' dynamo, which recovers an Earth-like large-scale magnetic field geometry and decadal changes, with control parameters that were pushed towards geophysical values ([Aubert et al., 2017](#)). Although according to the information from the dynamo model diffusion contributes less than induction and sub-grids effects to the decadal SV, it is nevertheless much larger than what could be expected from classical estimates of $Rm \approx 1000$. [Gillet et al. \(2019\)](#) argued that due to the presence of a magnetic boundary layer of thickness L_r , diffusion amounts to $\approx 10\%$ of the SV, which corresponds to $L_r = D/10 = 225$ km. Moreover, the 10% diffusion contribution to the SV applies to all degrees except the dipole for which it is even larger. Overall, these inverted core flow studies suggest that magnetic diffusion may contribute substantially to the observed SV.

Furthermore, [Metman et al. \(2019\)](#) constructed a purely diffusive evolution of the magnetic field to explain the observed decadal SV. Their model matched COV-OBSx.1 ensemble mean ([Gillet et al., 2015a](#)) within one standard deviation for periods up to 30 yr. The depth of the magnetic structure that influences the field at the CMB was found to be 10% of the shell ([Metman et al., 2019](#)).

Magnetic boundary layers are formed with both homogeneous and heterogeneous thermal boundary conditions. Heterogeneous boundary conditions were shown to localize magnetic flux patches, flow features and inner core boundary growth in some statistically preferred positions (e.g. [Olson and Christensen 2002](#); [Gubbins, 2003](#); [Aubert et al., 2007, 2008, 2013](#); [Gubbins et al., 2007, 2011](#); [Davies et al., 2008, 2009](#); [Takahashi et al., 2008](#); [Amit and Choblet, 2009, 2012](#); [Amit et al., 2015](#); [Olson et al., 2017, 2018](#); [Mound et al., 2019](#)). Recently, [Terra-Nova et al. \(2019\)](#) studied the impact of heterogeneous boundary conditions on the localization of the South Atlantic Anomaly (SAA). They showed that the anomaly is controlled by low CMB heat flux that yields a persistent upwelling below the South Atlantic.

Knowledge of the thickness of the magnetic boundary layer at the top of Earth's core is vital for understanding the role of diffusion in the geomagnetic SV and consequently for the interpretation of the SV in terms of core motions. The orientation of the horizontal field within this layer is linked to dynamo mechanisms and as such may point to locations of field generation. The lateral distribution of persistent magnetic boundary layers may shed light on how the heterogeneous lower mantle affects the geomagnetic field morphology.

In this paper we design a scheme to evaluate magnetic boundary layers and apply it to the upper part of the spherical shell of numerical dynamos. Note that such layers likely exist above the bottom boundary as well; however, because geomagnetic observations are accessible exclusively on the CMB, we focus here on the layers at the top of the shell. We analyze the depth and lateral distribution of the magnetic boundary layers, the field orientation within the layers and their dynamical origins. We propose scaling laws for the thickness of the

boundary layers and extrapolate (or interpolate) the results to Earth's core conditions. We also study the impact of mantle control on the locations of these layers. We finish with a discussion including geophysical implications.

2. Methods

2.1. Numerical dynamos

Numerical dynamo simulations are self-consistent solutions to the full set of magnetohydrodynamic equations: conservation of momentum, electromagnetic induction, conservation of heat (or co-density), incompressibility and non-existent magnetic monopoles. The Boussinesq approximation is applied, and gravity varies linearly with radial distance. These equations in non-dimensional form are respectively (e.g. [Olson et al., 1999](#); [Wicht, 2002](#)):

$$E \left(\frac{\partial \mathbf{u}}{\partial t} + \mathbf{u} \cdot \nabla \mathbf{u} - \nabla^2 \mathbf{u} \right) + 2\hat{z} \times \mathbf{u} + \nabla P = Ra^* \frac{\mathbf{r}}{r_o} C + \frac{1}{Pm} (\nabla \times \mathbf{B}) \times \mathbf{B}, \quad (2)$$

$$\frac{\partial \mathbf{B}}{\partial t} = \nabla \times (\mathbf{u} \times \mathbf{B}) + \frac{1}{Pm} \nabla^2 \mathbf{B}, \quad (3)$$

$$\frac{\partial C}{\partial t} + \mathbf{u} \cdot \nabla C = \frac{1}{Pr} \nabla^2 C, \quad (4)$$

$$\nabla \cdot \mathbf{u} = 0, \quad (5)$$

$$\nabla \cdot \mathbf{B} = 0, \quad (6)$$

where \mathbf{u} is the fluid velocity, t time, \hat{z} the direction of the axis of rotation, P the pressure, \mathbf{r} the position vector, r_o the outer boundary radius, C the co-density and \mathbf{B} the magnetic field. The co-density is given by $C = \alpha T + \beta \xi$ where T is temperature, ξ light elements concentration and α and β their respective expansivities. Eqs. (2)–(4) contain four (internal) control parameters. The Ekman number represents the ratio of viscous to Coriolis forces:

$$E = \frac{\nu}{\Omega D^2}. \quad (7)$$

The heat flux based Rayleigh number represents the convection vigor vs. retarding forces:

$$Ra = \frac{\alpha g_o q_o D^4}{\kappa \nu k}. \quad (8)$$

The Prandtl number and the magnetic Prandtl number are ratios of diffusivities:

$$Pr = \frac{\nu}{\kappa}, \quad (9)$$

$$Pm = \frac{\nu}{\eta}. \quad (10)$$

Note that the modified Rayleigh number in (2) Ra^* is related to the classical Rayleigh number in (8) Ra by $Ra^* = RaE/Pr$. In (7)–(10) Ω is the rotation rate, ν the kinematic viscosity, D the shell thickness, g_o the gravitational acceleration at the outer boundary, q_o the mean outer boundary heat flux, k the thermal conductivity, κ the thermal diffusivity and η the magnetic diffusivity.

We analyzed the same suite of dynamo models as [Terra-Nova et al. \(2019\)](#). They explored control parameters that produce dynamos with non-reversing dipole-dominated fields which roughly resemble Earth's field morphology during a chron. All dynamo simulations have rigid and electrically insulating conditions at both boundaries. The spherical shell has an Earth-like inner to outer core radii ratio of 0.35. No volumetric co-density source or sink was assigned. On the outer boundary of most of the simulations a heat flux pattern was imposed based on a tomographic model of seismic shear wave velocity anomalies at the

Table 1

Dynamo models setup and results.

CASE	Ra	Pm	q^*	N_r	l_{max}	Rm	Rm^{pol}	$\langle L_r \rangle$	ζ^{B_ϕ/B_θ}
$E = 3 \cdot 10^{-4}$									
1	$5 \cdot 10^5$	4	0.7	41	64	107	51	370.6	0.84
2	$1 \cdot 10^6$	4	0.7	41	64	166	84	323.7	0.70
3	$1 \cdot 10^6$	4	1.0	41	64	168	84	323.2	0.73
4	$1 \cdot 10^6$	9	0.7	41	64	356	189	276.9	0.66
5	$3 \cdot 10^6$	3	0.7	41	64	236	132	298.9	0.32
6	$3 \cdot 10^6$	4	0	41	64	368	220	204.2	-0.26
7	$3 \cdot 10^6$	4	0.7	41	64	312	175	277.4	0.35
8	$3 \cdot 10^6$	4	1.0	41	64	314	175	287.0	0.41
9	$3 \cdot 10^6$	9	0.4	41	64	248	87	326.3	0.94
10	$3 \cdot 10^6$	9	0.7	41	64	662	383	232.2	0.30
11	$3 \cdot 10^6$	9	1.0	41	64	677	387	236.2	0.24
12	$5 \cdot 10^6$	4	0.4	41	64	419	245	239.3	0.22
13	$5 \cdot 10^6$	4	0.7	41	64	428	247	241.1	0.23
$E = 1 \cdot 10^{-4}$									
14	$3 \cdot 10^6$	3	0.7	49	64	136	67	371.5	0.87
15	$3 \cdot 10^6$	4	0.7	49	64	178	90	338.3	0.77
16	$5 \cdot 10^6$	4	0.7	49	64	238	125	321.4	0.75
17	$1 \cdot 10^7$	4	0.7	49	64	350	193	290.7	0.65
18	$3 \cdot 10^7$	2	0	49	64	328	190	293.1	0.42
19	$3 \cdot 10^7$	2	0.4	65	96	331	190	297.3	0.23
20	$3 \cdot 10^7$	2	0.7	49	64	332	191	316.1	0.48
21	$3 \cdot 10^7$	2	1.0	65	96	332	189	304.7	0.47
22	$4 \cdot 10^7$	2	0.7	65	96	398	230	293.1	0.29
23	$4 \cdot 10^7$	2	1.0	65	96	405	234	309.3	0.45
$E = 3 \cdot 10^{-5}$									
24	$4 \cdot 10^7$	0.8	0	65	96	95	47	383.9	0.69
25	$4 \cdot 10^7$	0.8	0.4	65	96	100	49	387.8	0.67
26	$8 \cdot 10^7$	0.8	0.7	81	106	130	70	355.8	0.71
27	$8 \cdot 10^7$	0.8	1.0	81	106	131	70	352.8	0.64
28	$9 \cdot 10^7$	2	1.0	97	106	332	185	325.7	0.67

Control parameters E , Ra , Pm and q^* are defined in (7)–(11). In all models $Pr = 1$. The number of radial grid points in the shell is N_r , and l_{max} is the maximum spherical harmonic degree and order. The magnetic Reynolds numbers Rm (17) and Rm^{pol} (18) are calculated from the time-average kinetic energy (total and poloidal, respectively) in the shell. $\langle L_r \rangle$ is the mean thickness of the magnetic boundary layers (13). ζ^{B_ϕ/B_θ} (16) compares magnetic boundary layers associated with the two horizontal field components.

lowermost mantle ([Masters et al., 2000](#)) truncated at spherical harmonic degree and order 6. The amplitude of the imposed heat flux heterogeneity is quantified by

$$q^* = \frac{q_{max} - q_{min}}{2q_o}, \quad (11)$$

where q_{max} and q_{min} are the maximum and minimum heat flux respectively (e.g. [Olson and Christensen, 2002](#)). For the inner boundary fixed co-density was imposed.

The radial resolution in the models is set so that the Ekman boundary layer is captured by at least 5 radial grid points. As we will show, these Ekman layers are substantially thinner than the magnetic boundary layers in the models, hence the resolution of the simulations does not bias the determination of the magnetic boundary layers. For dynamo models control parameters, spatial resolution and some main output see [Table 1](#). The dynamo models were calculated using the Magic5.1 code ([Wicht, 2002](#); [Schaeffer, 2013](#)).

2.2. Identification and evaluation of magnetic boundary layers

We describe here our scheme based on quantitative criteria to identify and evaluate magnetic boundary layers. At each longitude/co-latitude pair (ϕ, θ) we search for the depth where peaks of horizontal field components B_ϕ and B_θ reside which we define as magnetic boundary layers (for an illustration see [Fig. 1](#)). Since we look for a layer below the outer boundary we restrict our search of peaks to the upper part of the shell of the dynamo models. We arbitrarily chose the upper

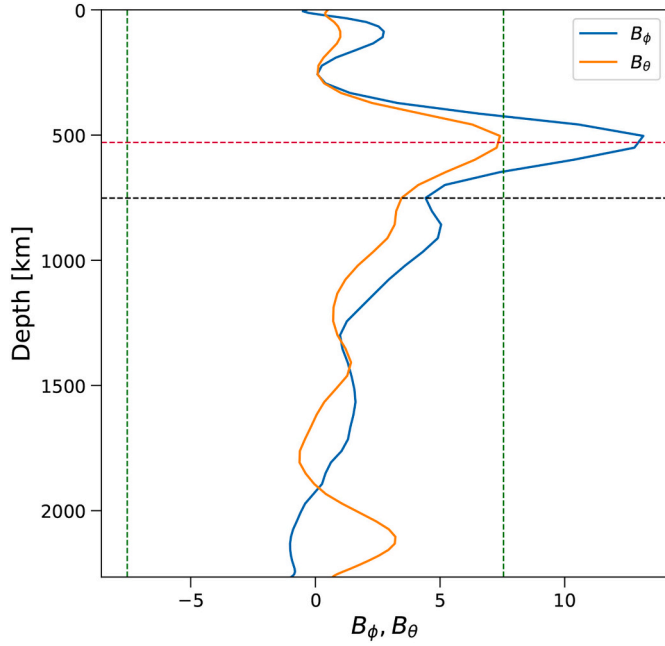


Fig. 1. Radial profiles of B_ϕ and B_θ at a single location for a snapshot of dynamo model 8. Horizontal black dashed line denotes the limit above which the magnetic boundary layers are considered. Vertical dashed green lines denote the threshold horizontal field values for defining a layer. Horizontal dashed red line is the off-grid peak horizontal field value assigned to L_r . (For interpretation of the references to colour in this figure legend, the reader is referred to the web version of this article.)

third of the shell, i.e. the top ≈ 750 km (horizontal dashed black line in Fig. 1). More specifically, our scheme follows these steps:

- I. For each radial profile of both B_ϕ and B_θ we determine a maximum, $|B_i|_{max}$, where i denotes either ϕ or θ .
- II. We restrict the analysis to radial profiles that obey $|B_i|_{max} > f|B_h^V|_{max}$, where f is a critical fraction (see subsection 2.2.2 below) and $|B_h^V|_{max}$ is the maximum horizontal field intensity in the upper third part of the shell (superscript V denotes volume). The vertical dashed green lines in Fig. 1 represent the horizontal field threshold for defining a layer $f|B_h^V|_{max}$. Note that in this example B_ϕ passes this criterion whereas B_θ does not pass it.
- III. We further exclude radial profiles where $|B_i|_{max}$ is the largest value but not a local maximum.
- IV. If conditions ii and iii are met, we use the depth of $|B_i|_{max}$ to determine the magnetic boundary layer thickness, L_r . In order to obtain a refined, off-grid value for the depth of the peak horizontal field, we fit a second order polynomial over the radial level of $|B_i|_{max}$ plus two levels above and two levels below it. The resulting peak is shown by the horizontal dashed red line in Fig. 1.
- V. We give a weight for each radial profile by

$$W = |B_h|_{max} \sin \theta. \quad (12)$$

where $|B_h|_{max}$ is the maximum horizontal field intensity in the radial profile. The first term assigns larger weight to peaks of more intense horizontal field. The second term is just a geometric correction to a uniform grid on a spherical surface. We evaluate the globally averaged magnetic boundary layer thickness as:

$$\langle L_r \rangle = \frac{\sum_j (L_r W)_j}{\sum_j W_j}, \quad (13)$$

where j may denote spatial summation over radial profiles of either a snapshot, a set of snapshots or a time average.

Note that we do not make any distinction between B_ϕ and B_θ

magnetic boundary layers in the $\langle L_r \rangle$ calculation (13) because the magnetic boundary layers correspond to the concentration of toroidal fields regardless of their orientation. The distinction is applied when calculating the positions of each field component because their dynamical origins are different (Olson et al., 1999; Aubert et al., 2008b).

2.2.1. Preferred locations

Due to the multiple-peak and rough histograms of longitude, a simple and single global weighted average as (13) cannot be applied to obtain multiple preferred longitudes. We therefore followed here the procedure of Terra-Nova et al. (2019). Briefly, we smoothed the longitude histograms of B_ϕ and B_θ by applying moving averages to avoid over interpretation of small-scale features related to the finite simulation time. Next we applied a cutoff in order to interpret only persistent peaks in these histograms. Then using second order polynomials centered at these prominent peaks (one polynomial for each peak), non-discrete preferred longitudes $\mathcal{P}_\theta^{B_\phi}$ and $\mathcal{P}_\theta^{B_\theta}$ were obtained for B_ϕ and B_θ magnetic boundary layers, respectively.

In latitude, B_ϕ distributions have a single peak close to the equator, thus it is simply obtained by

$$\mathcal{P}_\theta^{B_\phi} = \frac{\sum_j (\theta^{B_\phi} W)_j}{\sum_j W_j}. \quad (14)$$

The B_θ distributions in latitude show single mid-latitude peaks, one at each hemisphere. We thus obtain $\mathcal{P}_\theta^{B_\theta} (NH)$ and $\mathcal{P}_\theta^{B_\theta} (SH)$ by weighted averages similar to (14) but restricted to the Northern Hemisphere (NH) and Southern Hemisphere (SH), respectively.

The preferred longitudes $\mathcal{P}_\theta^{B_\phi}$ and $\mathcal{P}_\theta^{B_\theta}$, together with any deviation of $\mathcal{P}_\theta^{B_\phi}$ from 90° , describe the boundary control on the locations of magnetic boundary layers. Deviation from equatorial symmetry in $\mathcal{P}_\theta^{B_\theta}$ in the two hemispheres may also be considered as evidence for mantle control. However, B_θ latitudinal distributions are more challenging to interpret since $\mathcal{P}_\theta^{B_\theta}$ is unknown at homogeneous conditions.

2.2.2. Selection of threshold

The selection of the threshold f introduced in step ii (see section 2.2) is not straightforward. For a dynamo model with homogeneous outer boundary heat flux, if the simulation was run long enough, the longitudinal distribution of magnetic boundary layers is expected to become uniform and the latitudinal distribution is expected to become equatorially symmetric. We use these expected idealized properties of the homogeneous models to investigate the sensitivity of the results to the critical fraction f .

Following Terra-Nova et al. (2019), in longitude we estimate a typical histogram non-uniformity

$$h_w = \sqrt{\frac{1}{N_l} \sum_l ((H_\phi)_l - \bar{H}_\phi)^2}, \quad (15)$$

where H_ϕ are bin heights, \bar{H}_ϕ their average, l denotes summation over all bins and N_l is the number of longitude histogram bins. As in Terra-Nova et al. (2019), the bin size was selected following thorough empirical trials. The lower h_w the flatter the longitude histograms. In colatitude we monitor the sensitivity of the equatorial peak of the B_ϕ magnetic boundary layers (14) to f . Positive/negative values of $(90^\circ - \mathcal{P}_\theta^{B_\phi})$ correspond to more magnetic boundary layers in the Northern/Southern Hemisphere, respectively. In summary h_w and $(90^\circ - \mathcal{P}_\theta^{B_\phi})$ are expected to approach zero in the dynamo models with homogeneous outer boundary heat flux. In contrast, we have no constraints from homogeneous models on $\langle L_r \rangle$. Here we only search for low dependency of $\langle L_r \rangle$ on the critical fraction f .

2.2.3. Field orientation

Two different dynamo mechanisms produce magnetic boundary layers associated with the two different horizontal field components, B_ϕ

and B_θ (Olson et al., 1999; Aubert et al., 2008b). To compare these two effects quantitatively we calculate the following ratio based on the horizontal magnetic field components which define the respective boundary layers:

$$\zeta^{B_\phi/B_\theta} = \frac{\sum_j (W_\phi)_j - \sum_j (W_\theta)_j}{\sum_j (W_\phi)_j + \sum_j (W_\theta)_j} \quad (16)$$

where W_ϕ and W_θ are respectively the weights (12) of the associated B_ϕ and B_θ magnetic boundary layers. If $\sum_j (W_\phi)_j > \sum_j (W_\theta)_j$ then $\zeta^{B_\phi/B_\theta} \rightarrow 1$, whereas $\sum_j (W_\phi)_j < \sum_j (W_\theta)_j$ renders $\zeta^{B_\phi/B_\theta} \rightarrow -1$ and in the case of $\sum_j (W_\phi)_j \approx \sum_j (W_\theta)_j$ the ratio $\zeta^{B_\phi/B_\theta} \rightarrow 0$. Thus ζ^{B_ϕ/B_θ} quantifies the relative contributions of B_ϕ and B_θ to the magnetic boundary layers.

2.3. Scaling laws

We investigate the relation between the magnetic boundary layer thickness (13) obtained in about twenty arbitrarily sampled snapshots vs. two versions of the magnetic Reynolds number. The first follows the classical definition (1), i.e. based on the total kinetic energy in the shell E_{kin} ,

$$Rm = Pm \sqrt{2E_{kin}} \quad (17)$$

while the second is based on the poloidal kinetic energy E_{kin}^{pol} (i.e. on the poloidal flow magnitude) by

$$Rm^{pol} = Pm \sqrt{2E_{kin}^{pol}}. \quad (18)$$

The latter is advantageous because the magnetic boundary layers are formed by upwellings (Bloxham, 1986; Troyano et al., 2020) whose amplitudes are represented by the poloidal flow. On the other hand, application to Earth's core is more straightforward with (17) because the magnitude of the total core flow is rather well known from the geomagnetic SV (Finlay and Amit 2011; Holme 2015) whereas the poloidal flow magnitude is highly debated (see Huguet et al., 2018; Olson et al., 2018, and references therein). Using some analytical examples of rotating convection, Amit and Olson (2004) obtained ratios that correspond to $U^{pol}/U^{tor} \approx 0.1 - 0.4$, i.e. $U^{pol}/U \approx 0.1 - 0.3$ ('tor' superscript denoting toroidal flow). In most core flow models the poloidal flow is about an order of magnitude smaller than the toroidal, i.e. $U^{pol}/U^{tor} \sim 0.1$ (Finlay and Amit 2011). Based on these estimates, results were extrapolated (or interpolated) to Earth's core conditions.

We searched for power law fits to the magnetic boundary layer thickness $\langle L_r \rangle$ (13) vs. Rm (17) and Rm^{pol} (18). These power laws by definition satisfy infinitely thin layers for infinitely large flow magnitudes. A linear fit was obtained for $\langle L_r \rangle$ vs. the parameter defining the horizontal field orientation within the magnetic boundary layer ζ^{B_ϕ/B_θ} (16). In addition, more generic power law fits were obtained for $\mathcal{P}_\theta^{B_\phi}$ vs. the dynamo control parameters (7)–(11). For all empirical fits involving extrapolation or interpolation to Earth-like conditions we included error estimates based on the standard deviation σ of the vertical distance between the results and their fit (see Aubert et al., 2009). We plotted best-fit laws with their 2σ error lines which correspond to more than 95% of the data if the error distribution is normal.

3. Results

3.1. Depth and lateral distribution

We start with an example of a complete analysis of one snapshot from a dynamo model. Figs. 2a and b show the radial profiles of B_ϕ and B_θ that passed the criteria (subsection 2.2) in a snapshot from dynamo model 8. The positions of these profiles on the globe as well as their associated thicknesses are given in Fig. 2c and d for B_ϕ and B_θ , respectively. Regions absent of layers appear either where there is no upwelling flow or where the deep-seated toroidal field is weak. The roughly bell-shape depth histogram in Fig. 2e indicates that in this

snapshot the horizontal field peaks at around 300 – 500 km, most notably for the ϕ component (Fig. 2a), with a global mean of $\langle L_r \rangle = 346.27$ km in this snapshot. Figs. 2c, d and f point to multiple preferred longitudes in this particular snapshot, below Africa, Oceania and to a lesser extent the Pacific for B_ϕ magnetic boundary layers and below America and East Asia for B_θ layers. Figs. 2c, d and g show a preferred equatorial location for B_ϕ magnetic boundary layers whereas preferred mid-latitude locations are found at both hemispheres for B_θ layers with higher histogram peaks in the Northern Hemisphere for both horizontal components. We will later show that the tendency in this snapshot to have more layers in the north is in fact persistent.

Fig. 2 was obtained using a critical threshold of $f = 0.5$. We test the sensitivity of our results to this critical fraction by monitoring the typical non-uniformity of the longitude histogram h_w , the preferred co-latitude of the azimuthal field $\mathcal{P}_\theta^{B_\phi}$ and the mean magnetic boundary layer thickness $\langle L_r \rangle$ for time averages (left panel of Fig. 3) and snapshots (right panel of Fig. 3) of three dynamo models with homogeneous outer boundary heat flux and different E values as well as one model with heterogeneous outer boundary heat flux. For both time averages and snapshots h_w increases sharply when f reaches its highest values (strongest selection). On the other hand, the h_w values of the time-average homogeneous models exhibit an asymptotic behavior for $f = 0.2 - 0.5$ with h_w approaching zero and is nearly f -independent (Fig. 3a), whereas for the heterogeneous model h_w increases for all f . For snapshots, in both homogeneous and heterogeneous models h_w increases for all values of f (Fig. 3b). $\mathcal{P}_\theta^{B_\phi}$ values have a similar asymptotic behavior as h_w for $f = 0.2 - 0.6$ for time averages of homogeneous models, i.e. $\mathcal{P}_\theta^{B_\phi}$ approaches 90° and is f -independent. In contrast, the time-average heterogeneous model shows the effects of the imposed heat flux. The co-latitude peaks away from the equator (in the Northern Hemisphere) and $\mathcal{P}_\theta^{B_\phi}$ varies substantially with f (Fig. 3c). In snapshots, envelopes of $\mathcal{P}_\theta^{B_\phi}$ vs. f are seen for each model, with the thickness of the envelope increasing with f . This increase is mild for f values between 0.2 – 0.5 (Fig. 3d). Similarly and most importantly for our purposes, values of $\langle L_r \rangle$ remain weakly sensitive to f in the entire range of f for time averages and in the range $f = 0.2 - 0.4$ for snapshots (Figs. 3e and f, respectively). Overall, f needs to be large enough to guarantee that only intense horizontal fields are considered, but it also needs to be small enough to verify that the results are sufficiently insensitive to this choice. We choose f in between the largest value where $\langle L_r \rangle$ still has an asymptotic behavior for both snapshots and time averages and the largest value with an asymptotic behavior of h_w and $\mathcal{P}_\theta^{B_\phi}$ for time averages. Thus, $f = 0.5$ seems a sensible choice for both snapshots and time averages of the dynamo models.

Fig. 4a and b shows the stacked positions and depths of the radial profiles of B_ϕ and B_θ , respectively, in all snapshots from a dynamo model with imposed heterogeneous outer boundary heat flux using $f = 0.5$. Relatively shallow magnetic boundary layers associated with B_θ (see the triangles in Fig. 4b) are found at mid latitudes, while in the equatorial region mostly deeper layers associated with B_ϕ are observed (see the circles in Fig. 4a). The depth histogram shows a clear bell-shape distribution for the magnetic boundary layers thickness with $\langle L_r \rangle \approx 297.3$ km (black dashed line in Fig. 4c) given by (13). Table 1 summarizes the results for the stack of all snapshots. The values of $\langle L_r \rangle = 204.2 - 389.1$ km are at mid depth, far from either the prescribed limit of 750 km depth and the outer boundary, farther from the former. In longitude, three peaks are found for B_ϕ magnetic boundary layers $\mathcal{P}_\theta^{B_\phi}$: 167.0° W (Pacific Ocean), 11.6° W (Atlantic ocean) and 115.8° E (Australia) (see green vertical lines in Fig. 4d). Two longitudinal peaks are found for B_θ magnetic boundary layers $\mathcal{P}_\theta^{B_\theta}$: 55.7° W (South America) and 82.5° E (Indian Ocean) (see purple vertical lines in Fig. 4d). In latitude, the equatorial tendency of B_ϕ layers is clear with $\mathcal{P}_\theta^{B_\phi} = 90.6^\circ$ (green vertical line in Fig. 4e) while the mid-latitudes peaks of B_θ layers $\mathcal{P}_\theta^{B_\theta} = 47.8^\circ$ and 130.4° are both close to $\approx 40^\circ$ off the equator (purple vertical lines in Fig. 4e).

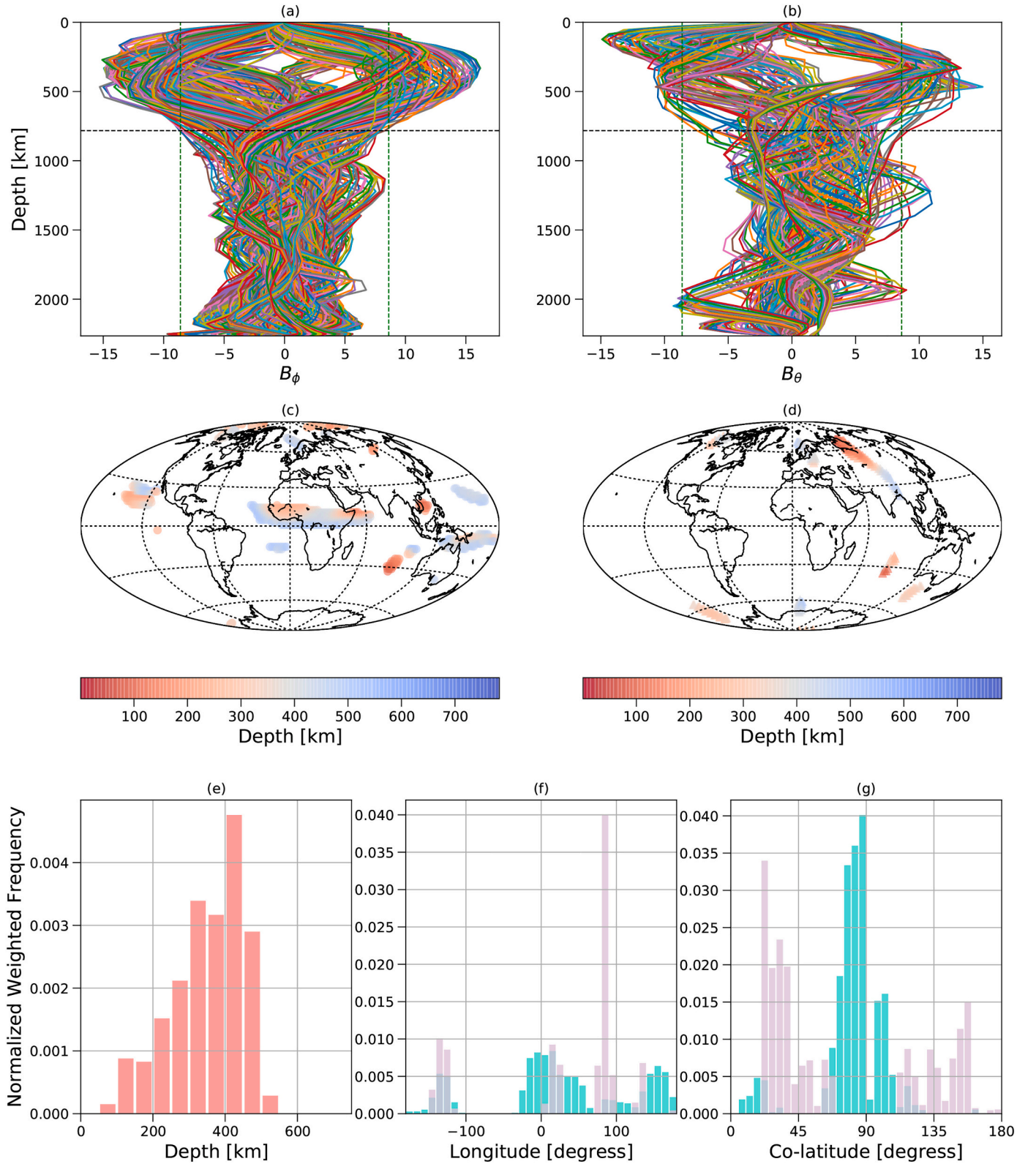


Fig. 2. Magnetic boundary layer distribution in a snapshot of dynamo model 8 for $f = 0.5$. (a) and (b) are the radial profiles of B_ϕ and B_θ that passed the criteria, respectively. (c) and (d) show the position on the globe and depth of the extrema of the radial profiles in (a) and (b), respectively. (e)-(g) show the histograms of depth, longitude and co-latitude of extrema of the radial profiles, respectively. Horizontal dashed black lines in (a) and (b) denote the limit above which the magnetic boundary layers are considered and vertical dashed green lines denote the threshold horizontal field values for defining a layer. Circles/triangles in (c) and (d) correspond to B_ϕ and B_θ , respectively. Green/purple in (f) and (g) correspond to B_ϕ and B_θ , respectively. (For interpretation of the references to colour in this figure legend, the reader is referred to the web version of this article.)

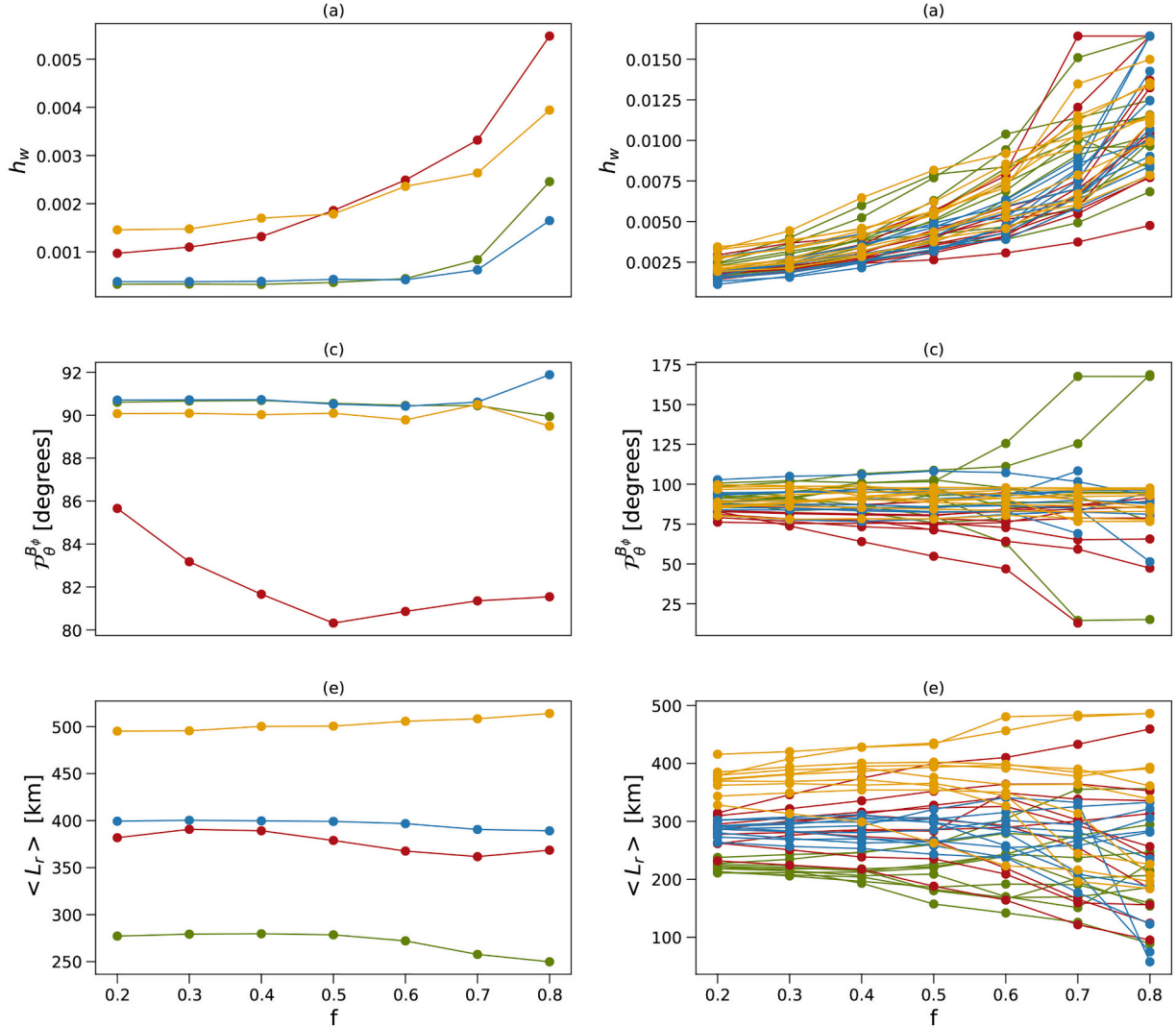


Fig. 3. Values of h_w , $P_\theta^{B_\phi}$ and $\langle L_r \rangle$ vs. f for time averages (left) and snapshots (right) of three dynamo models with homogeneous outer boundary heat flux for different Ekman numbers: Green lines for $E = 3 \cdot 10^{-4}$ (case 6), blue lines for $E = 1 \cdot 10^{-4}$ (case 18) and yellow lines for $E = 3 \cdot 10^{-5}$ (case 24). Also shown a dynamo model with heterogeneous outer boundary heat flux and $E = 3 \cdot 10^{-4}$ (red lines, case 8). (For interpretation of the references to colour in this figure legend, the reader is referred to the web version of this article.)

Fig. 5 shows moving averages of the latitudinal histograms (e.g. Fig. 4e) for B_θ magnetic boundary layers of all models. Peak B_θ layers at mid latitudes of each hemisphere (vertical lines in Fig. 5) are in agreement with the magnetic anticyclones of Aubert et al., 2008b. The peaks range from 23° to 58° N and 28° to 66° S with a mean of 40° N and 41° S. The distance between the NH/SH peaks of the same model vary from 62° to 107°, with a mean for all models of 82°.

We fit power laws for the thickness of the magnetic boundary layers $\langle L_r \rangle$ (13) as a function of the conventional magnetic Reynolds number (17) as well as vs. that based on the poloidal flow (18) (Fig. 6). For both Rm and Rm^{pol} the fitted slopes are negative, i.e. the faster the flow the thinner the magnetic boundary layer, as expected (Bloxham, 1986; Troyano et al., 2020). Extrapolation to $Rm = 1000$ gives $\langle L_r \rangle \approx 220$ km (Fig. 6 left), whereas interpolation to $Rm^{pol} = 100 - 300$ (Amit and Olson 2004; Huguet et al., 2018) gives $\langle L_r \rangle \approx 260 - 330$ km (Fig. 6 right) for the magnetic boundary layer thickness of the Earth.

3.2. Dynamical origin

We demonstrate the dynamical origin of the magnetic boundary

layers using equatorial and meridional slices of the flow and the horizontal field. Figs. 7a and b show equatorial slices of B_ϕ and B_θ for a snapshot of dynamo model 11. Here the concentration of horizontal magnetic field at the outer part represents magnetic boundary layers in the equatorial region. Pronounced magnetic boundary layers associated with B_ϕ are found in this snapshot at longitudes $\approx 90^\circ\text{W}$, 135°W , 55°E and 120°E (Fig. 7a). Note the east-west elongation of these intense B_ϕ structures close to the outer boundary (as in Aubert et al., 2008b). In contrast, B_θ is weaker at the equatorial plane, especially close to the outer boundary. Upwelling and downwelling of fluid are inferred from pairs of elongated opposite-sign structures of axial vorticity, w_z (Fig. 7c). Remarkable upwelling/downwelling structures that extend from deep within the shell at longitudes $\approx 90^\circ\text{E}$, 85°W and 120°W (Fig. 7c) are in the vicinity of magnetic boundary layers associated with B_ϕ (Fig. 7a).

Fig. 8 shows again equatorial slices but for a different snapshot of the same model. Fig. 8a shows a massive magnetic boundary layer below almost the entire equatorial region of the Pacific hemisphere. Note that here no corresponding large scale upwelling/downwelling is seen (Fig. 8c). This demonstrates that field features in general and magnetic boundary layers in particular may often linger after their

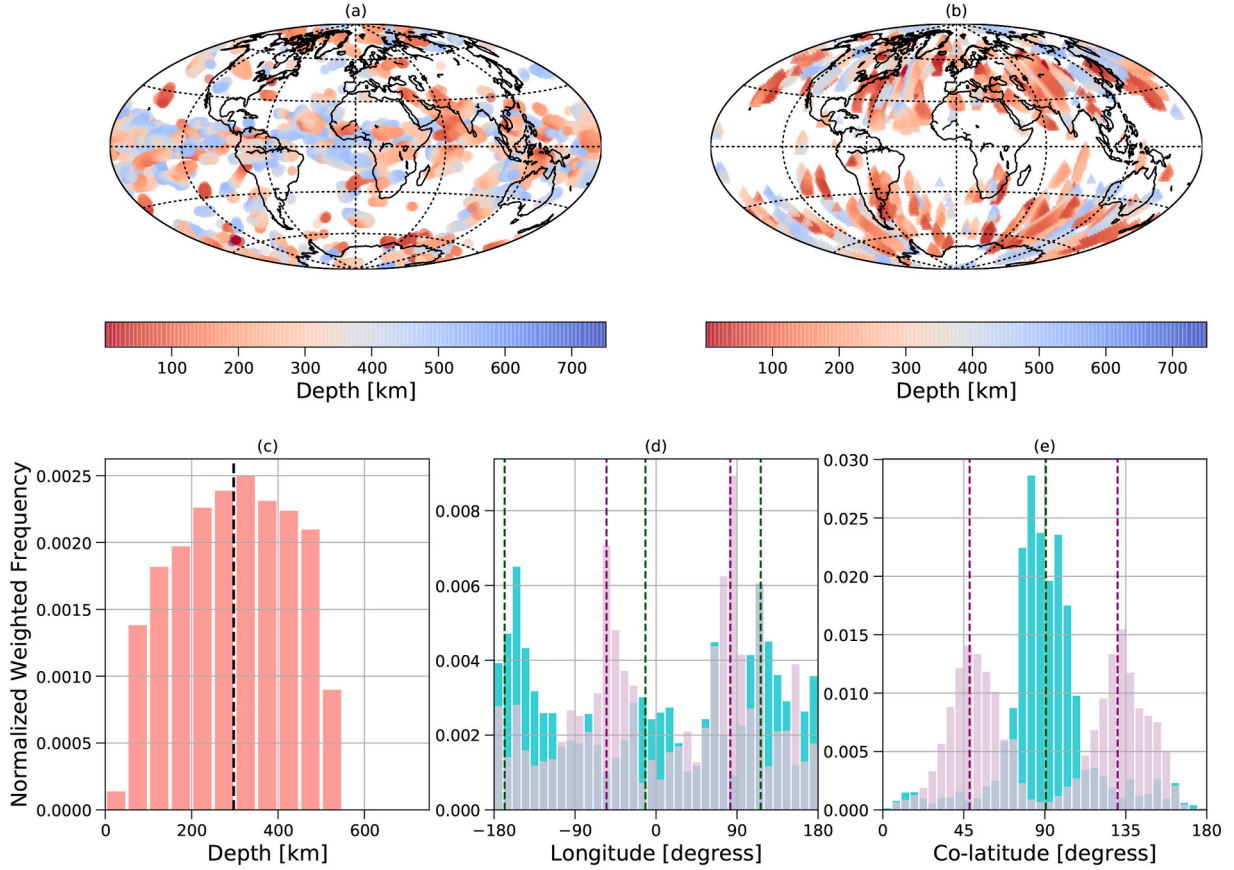


Fig. 4. As in Fig. 2 for a stack of all snapshots of dynamo model 19 using $f = 0.5$. In this model $\langle L_r \rangle \approx 297.3$ km, $\varphi_\phi^{B\phi} = 167.0^\circ$ W, 11.6° W and 115.8° E, $\varphi_\theta^{B\theta} = 55.7^\circ$ W and 82.5° E, $\varphi_\phi^{B\theta} = 90.6^\circ$ and $\varphi_\theta^{B\theta} = 47.8^\circ$ and 130.4° (see vertical dashed lines).

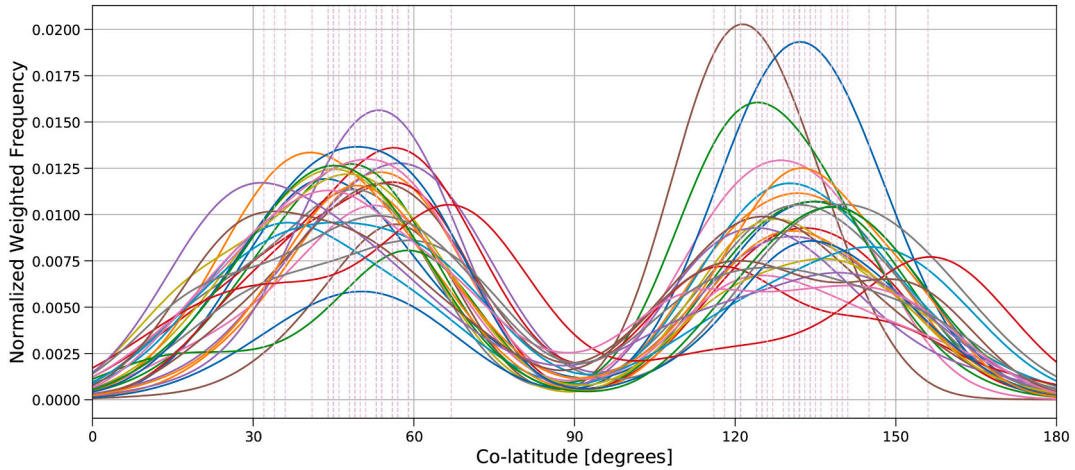


Fig. 5. Moving averages of B_θ histograms vs. co-latitude for all dynamo models. Dashed vertical lines denote the peaks $\varphi_\theta^{B\theta}$ (NH) and $\varphi_\theta^{B\theta}$ (SH) (defined in section 2.2.1). Each colour represents a model.

forming flow structures have evolved. Again B_θ is much less intense at the equator near the outer boundary, except for a smaller structure below the Pacific at $\approx 175^\circ$ E (Fig. 8b).

While Figs. 7 and 8 highlight equatorial magnetic boundary layers associated with B_ϕ , at mid latitudes these layers are often associated with B_θ (Figs. 2 and 4). Figs. 9a and b show meridional slices of the horizontal field components at a selected longitude in a snapshot from dynamo model 8. Again a magnetic boundary layer associated with B_ϕ is found at the equatorial region (Fig. 9a) where a vast (though relatively weak) upwelling appears (Fig. 9c). However, magnetic boundary

layers associated with B_θ at mid latitudes are also seen. In particular, a strong B_θ structure appears outside the intersection of the tangent cylinder (Aurnou et al., 2003) with the northern hemisphere outer boundary (Fig. 9b) where a particularly strong upwelling structure resides (Fig. 9c).

Fig. 10 shows the dependence of the mean thickness of the magnetic boundary layers $\langle L_r \rangle$ on the quantity that represents the partitioning of horizontal field orientations $\zeta^{B\phi/B\theta}$ (16) for all dynamo models. The larger the values of $\langle L_r \rangle$ the more B_ϕ dominates over B_θ in the magnetic boundary layers. Table 1 and Fig. 10 show that with the

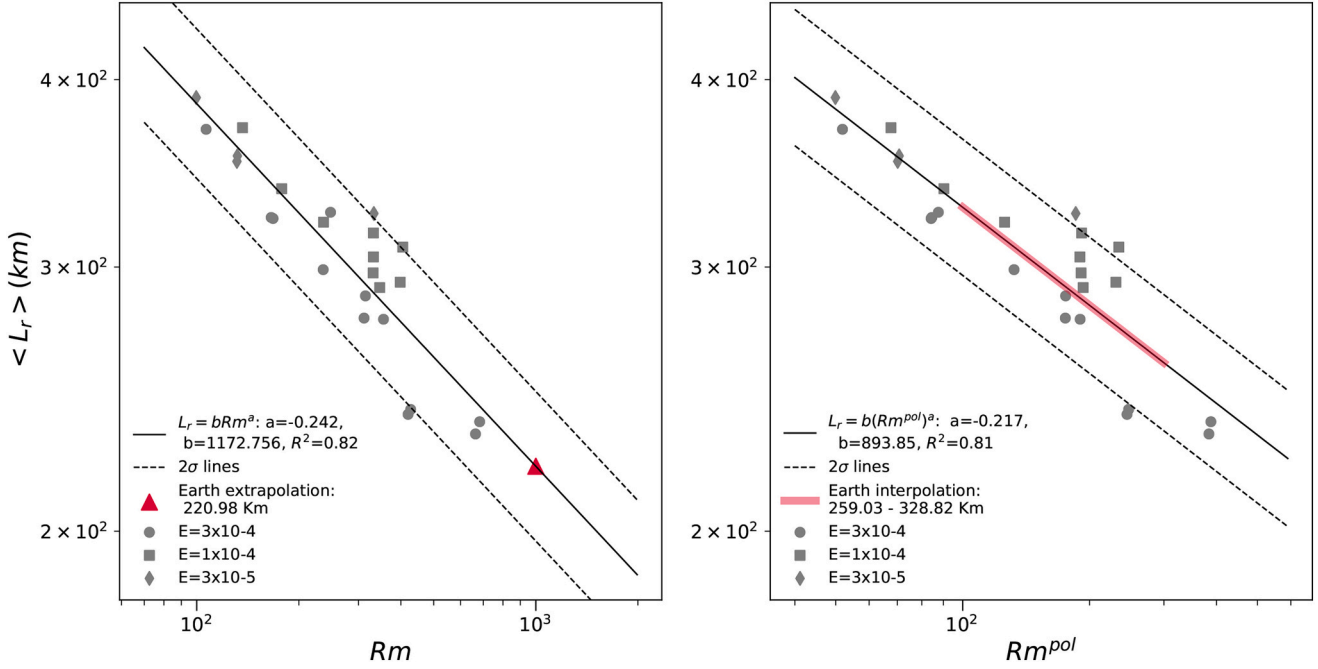


Fig. 6. Power law fits for the magnetic boundary layers thickness in the dynamo models as functions of Rm (left) and Rm^{pol} (right). Grey lines denote fits. Red triangles and thick red lines denote extrapolated (left) and interpolated (right) values to Earth-like conditions, respectively. The goodness of fits are measured by R^2 . Dashed lines denote 2σ error lines (see subsection 2.3). Dynamo models with different E values are denoted by different symbols (see legend). (For interpretation of the references to colour in this figure legend, the reader is referred to the web version of this article.)

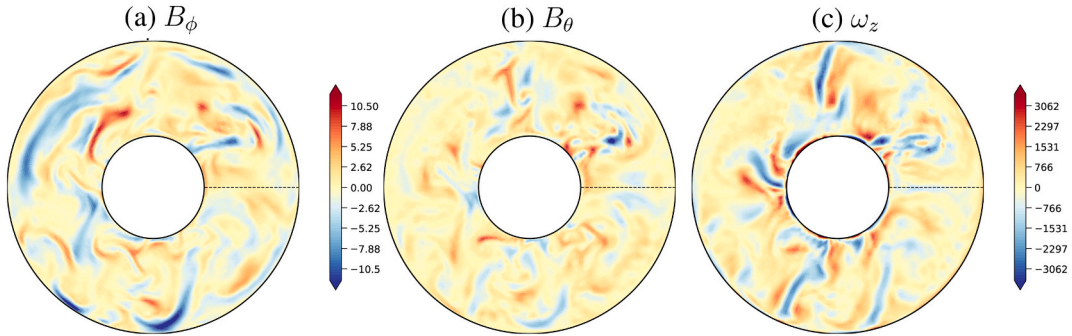


Fig. 7. Equatorial slices of B_ϕ (a), B_θ (b) and ω_z (c) in a snapshot of dynamo model 11. Dotted lines denote $\phi = 0^\circ$. The horizontal magnetic field components have the same colour scale.

exception of one dynamo model, ζ^{B_ϕ/B_θ} is positive, indicating that B_ϕ layers dominate over B_θ layers (16). In addition, ζ^{B_ϕ/B_θ} exhibits large variability from 0.22 to 0.94. For the $\langle L_r \rangle$ values based on the extrapolated (or interpolated) Rm and Rm^{pol} for the Earth, we obtain $\zeta^{B_\phi/B_\theta} \approx -0.07$ and $\zeta^{B_\phi/B_\theta} \approx 0.19 - 0.67$, respectively (Fig. 10). These results suggest that in Earth's outer core the magnetic boundary layers

either exhibit a balanced distribution of equatorial B_ϕ layers with mid-latitude layers associated with B_θ or mostly associated with B_ϕ .

3.3. Mantle control

We compare preferred locations of magnetic boundary layers with

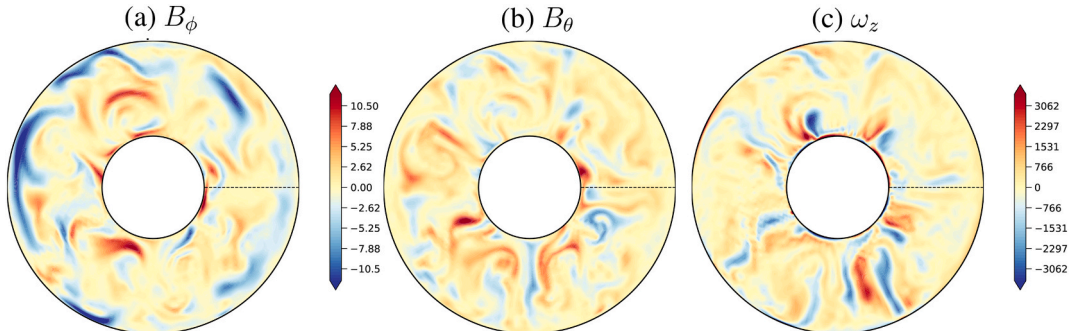


Fig. 8. As in Fig. 7 for a different snapshot of the same dynamo model.

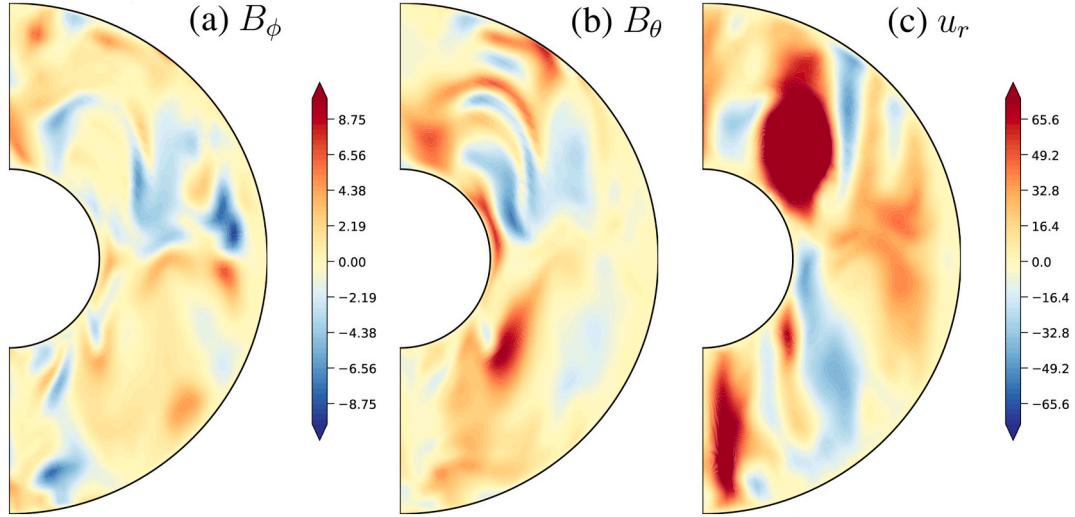


Fig. 9. Meridional slices of B_ϕ (a), B_θ (b) and the radial velocity (c) in a snapshot from dynamo model 8. The horizontal magnetic field components have the same colour scale.

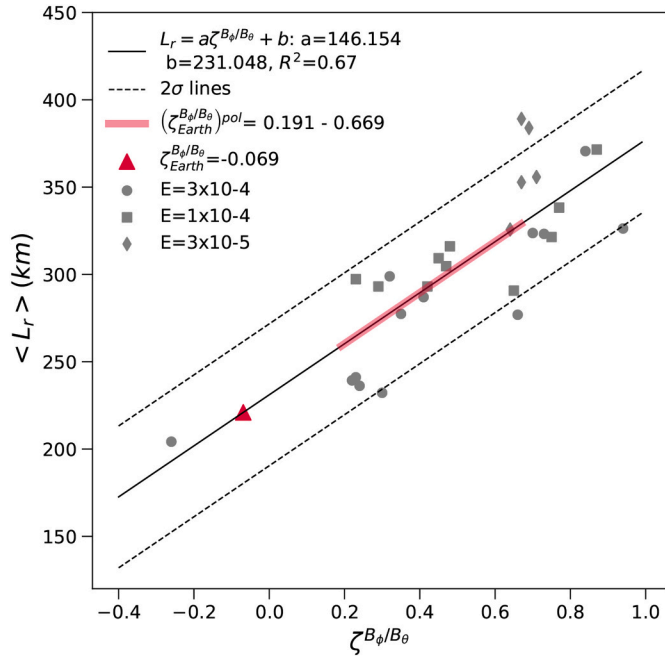


Fig. 10. Magnetic boundary layer thickness, $\langle L_r \rangle$ (13) vs. the ratio of horizontal field orientation, ζ^{B_ϕ/B_θ} (16). Grey line denotes linear fit. Red triangle and thick red line denote extrapolated/interpolated values to Earth-like conditions based on Rm (17) and Rm^{pol} (18), respectively. The goodness of fit is measured by R^2 . Dashed lines denote 2σ error lines (see subsection 2.3). Dynamo models with different E values are denoted by different symbols (see legend). (For interpretation of the references to colour in this figure legend, the reader is referred to the web version of this article.)

the distribution of outer boundary heat flux which we imposed as a boundary condition on the dynamo simulations. Figs. 11a and b show the meridional and zonal averages of the heat flux anomaly at the outer boundary. The meridional average has maxima at $\approx 70^\circ W$ and $120^\circ E$ and minima at $\approx 160^\circ W$ and $0^\circ E$. The zonal average has maxima at $\approx 45^\circ N$ and the south pole (though the latter represents a small area thus should not be overinterpreted) and a minimum at $20^\circ S$.

The effects of mantle control are first analyzed using the time averages of the dynamo models. Fig. 12 is much more straightforward to interpret than e.g. Fig. 2. Here the magnetic boundary layers are

exclusively equatorial associated with B_ϕ (Fig. 12a). Their lateral distribution correlates with low CMB heat flux (minima in Fig. 11a) associated with the African and Pacific Large Low Shear wave Velocity Provinces (LLSVPs). The histogram of $\langle L_r \rangle$ is very narrow, reflecting small dispersion of values, with a mean value of 251 km. Note that the magnetic boundary layers clearly appear at the Northern Hemisphere, providing convincing evidence for north-south asymmetry driven by lower mantle heterogeneity. The mean magnetic boundary layer thicknesses $\langle L_r \rangle$ based on the time-average field are larger than those for the stack of snapshots (see Table 1) because in the time-average analysis the layers associated with B_θ (which are thinner) are averaged out (ζ^{B_ϕ/B_θ} for the time-average field is 1.00 for all models expect one).

Because some meaningful magnetic boundary layers average out when analyzing the time-average field, in particular mid-latitude layers associated with B_θ , we focus on analyses of stacks of snapshots. Fig. 13 shows moving averages of the longitudinal histograms (e.g. Fig. 4d) for B_ϕ (a) and B_θ (b) magnetic boundary layers for all dynamo models. Most of the B_ϕ peaks are spread around $\approx 0^\circ$ and $\approx 180^\circ E$ (Fig. 13a). In contrast, B_θ peaks are more concentrated, centered around $\approx 90^\circ W$ and $\approx 90^\circ E$ (Fig. 13b). Overall, for each component the two peaks are separated by roughly 180 degrees. In addition, in most dynamo models the B_ϕ peaks are about 90 degrees away from the B_θ peaks.

Finally, we examine whether the outer boundary heat flux heterogeneity induces asymmetry between the northern and southern hemispheres in terms of the magnetic boundary layers. We fit a scaling law for $\mathcal{P}_\theta^{B_\phi}$ (14) vs. the control parameters (Fig. 14). The intercept at $\approx 91^\circ$ degrees is very close to the equator, without forcing the fit. This result is sensible since with no mantle control the peak is practically equatorial as expected. Note that $\mathcal{P}_\theta^{B_\phi}$ reaches more than 10° off the equator, in almost all cases in the northern hemisphere. The positive q^* power indicates that the larger the amplitude of the outer boundary heat flux heterogeneity the farther from the equator the magnetic boundary layers. The positive E power suggests that fast rotation promotes equatorial layers. The Ra and Pm powers are smaller hence caution is required in their interpretation. Nevertheless, qualitatively, the positive Ra power corresponds to strong main convection promoting deviation of layers from the equator. Overall, equatorial symmetry is broken by larger amplitude heat flux heterogeneity, weaker rotation and stronger convection, as expected. Less trivial is the tendency of low-latitude B_ϕ magnetic boundary layers to the north as revealed by our results, both when stacks of snapshots are analyzed (Fig. 14) as well as when the time-average field is processed (Fig. 12).

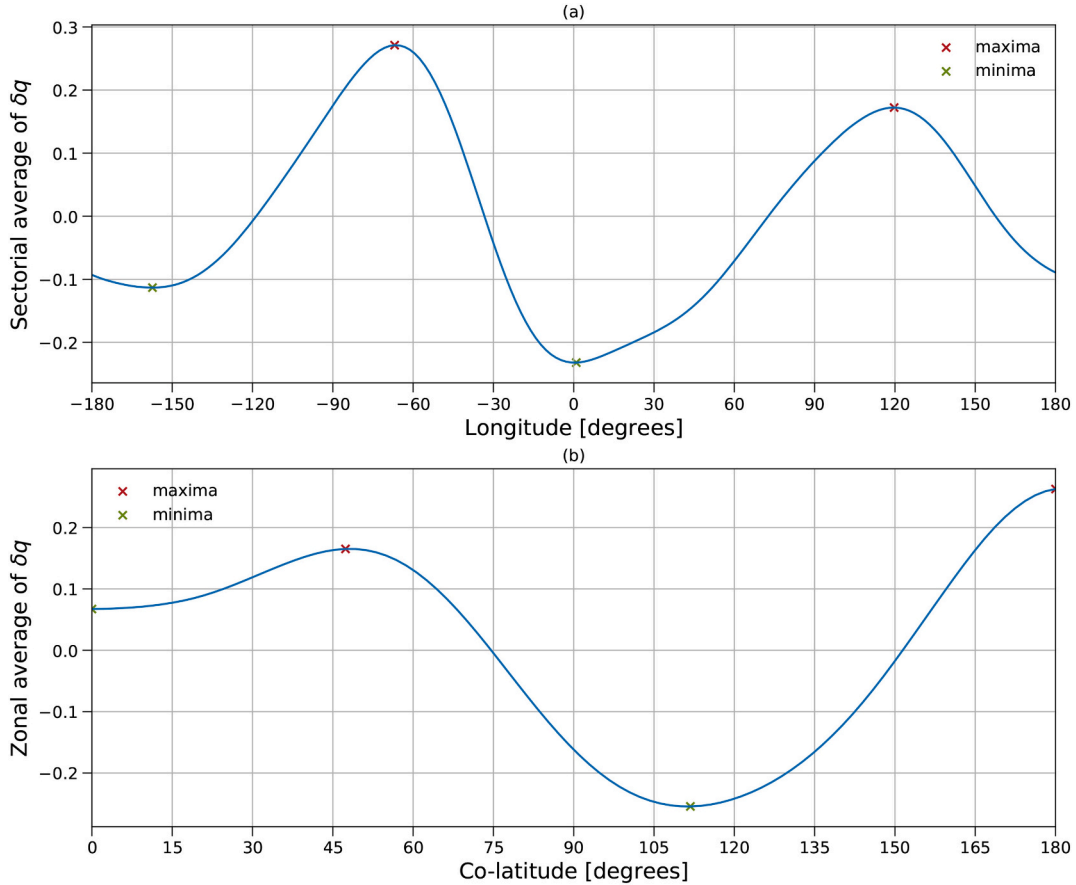


Fig. 11. Non-dimensional meridional (a) and zonal (b) averages of the imposed outer boundary heat flux anomaly.

4. Discussion

Numerical dynamo models with heterogeneous outer boundary heat flux inferred from a lowermost mantle tomography model were analyzed in order to evaluate the thickness and geographical distribution of magnetic boundary layers at the top of the shell. The simulations span different combinations of control parameters, including the amplitude of the imposed outer boundary heat flux heterogeneity. Based on the locations of intense horizontal fields in the shell, we carried out a scheme for the identification and evaluation of magnetic boundary layers. The peaks of radial profiles of B_ϕ and B_θ (Figs. 2a and b) were assigned as magnetic boundary layer depths. The intensities of the identified horizontal fields were integrated to calculate the mean magnetic boundary layer thickness $\langle L_r \rangle$. In the dynamo models, the magnetic boundary layer thicknesses range $\approx 200 - 400$ km (Table 1).

Previous estimates of the magnetic boundary layer thickness relied on different approaches. Amit and Christensen (2008) found in numerical dynamos that the ratio of the magnitudes of the radial to horizontal diffusion SV scales with the convective supercriticality. Extrapolating this ratio to Earth-like conditions, they obtained an effective magnetic Reynolds number of about 1 – 10 corresponding to a layer thickness of about 70 – 225 km. Chulliat and Olsen (2010) used two geomagnetic field snapshots based on satellite data to estimate the magnetic boundary layer thickness from the intensification of reversed flux surrounded by a radial field null-curve on the CMB. For $\eta = 1 \text{ m}^2\text{s}^{-1}$, they estimated a layer thickness of about 40 km. Considering the similarity between reversed flux patches histograms of longer (9 kyr) and shorter (3 kyr) periods of archeomagnetic field models, Terra-Nova et al. (2016) suggested 3 kyr as an upper bound to an effective magnetic diffusion time. Again for $\eta = 1 \text{ m}^2\text{s}^{-1}$ this corresponds to a layer thickness of about 310 km. Gillet et al. (2019) inferred from an

Earth-like high resolution dynamo model 10% diffusion contribution to the SV which corresponds to a layer thickness of about 225 km. Interestingly, Metman et al. (2019) proposed the same value based on a distinctive approach. They inverted for the 3D structure of the magnetic field which can explain the SV entirely by diffusion in the absence of any core flow. Their results are sensitive to the same 225 km layer below the CMB.

In our models $\langle L_r \rangle$ decreases with increasing magnetic Reynolds number (Fig. 6), i.e. stronger flow advects the magnetic boundary layer closer to the outer boundary (Bloxxham, 1986; Troyano et al., 2020). Extrapolation and interpolation to Earth's core conditions using $Rm = 1000$ and $Rm^{pol} = 100 - 300$ (Amit and Olson, 2004; Huguet et al., 2018) give $\langle L_r \rangle \approx 220$ km and $\approx 260 - 330$ km, respectively, in general agreement with the recent $\langle L_r \rangle$ estimates (Terra-Nova et al., 2016; Gillet et al., 2019; Metman et al., 2019). Our $\langle L_r \rangle$ estimates thus provide a vital insight into the magnetic structure of the deep core.

We further explored the control parameters dependence of our magnetic boundary layers thickness $\langle L_r \rangle$ by fitting power laws with E or Pm . Table 2 shows the results of these fits. Inclusion of E improves the fits more than inclusion of Pm . Overall, however, the powers of Rm or Rm^{pol} are 4–7 times greater than those of E (and even more so than those of Pm), indicating that the magnetic Reynolds numbers may explain most of the model dependence of the boundary layer thickness. Nevertheless, the negative powers of E suggest that faster rotation leads to thicker layers, while the negative powers of Pm indicate that more electrically conductive liquid core leads to thinner layers.

Obviously, the robustness of our results depends on our algorithm to identify and quantify the thickness of the magnetic boundary layers. It is possible that the algorithm fails to capture some layers. Nevertheless, the encouraging correlation between the mean magnetic boundary

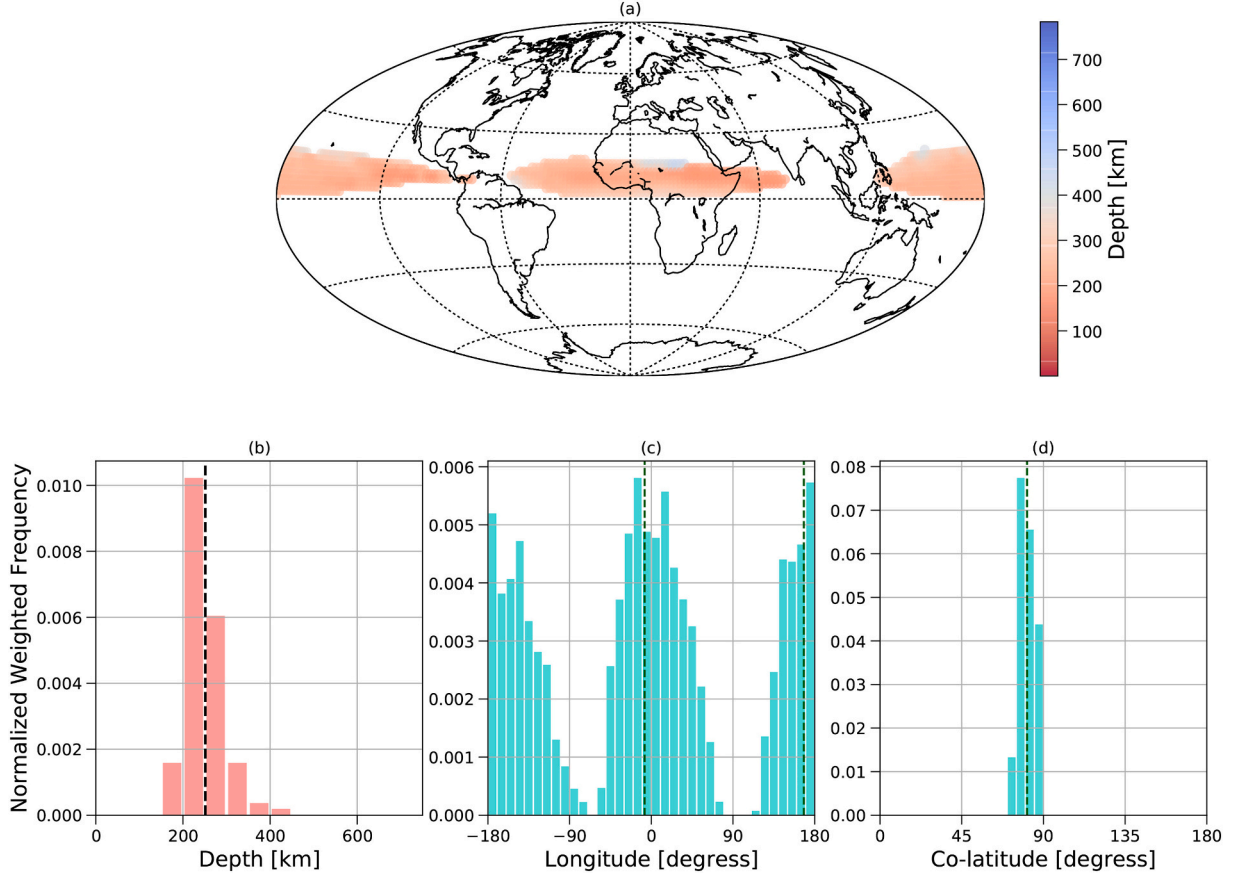


Fig. 12. As in Fig. 2 for the time-average of case 11 using $f = 0.5$. Here $\langle L_r \rangle \approx 251.4$ km, $\mathcal{P}_\phi^{B_\phi} = 7.4^\circ$ W and 168.0° E and $\mathcal{P}_\theta^{B_\theta} = 80.9^\circ$.

layer thickness and the magnetic Reynolds numbers (Fig. 6) suggests that $\langle L_r \rangle$ indeed represents the layers thickness.

We found two types of magnetic boundary layers classified by their field orientation, latitude and generating dynamo mechanism: One associated with B_ϕ at the equatorial region, the other associated with B_θ at mid latitudes (Figs. 2 and 4). Associated convective structures that expel toroidal fields towards the outer boundary are often identified (Figs. 7 and 9) though not always (Fig. 8) as the flow may evolve after the magnetic boundary layer has been formed. The two types of magnetic boundary layers that we identified are in agreement with dynamo mechanisms that were previously put forward in numerical dynamo models with dominant columnar convection (Olson et al., 1999; Aubert et al., 2008b). Cyclones associated with outer boundary high-latitude downwellings lead to flow divergence in the equatorial plane which expels B_ϕ magnetic boundary layers at the equator. Anti-cyclones are associated with outer boundary high-latitude upwellings which expel B_θ at mid to high latitudes adjacent to the columnar flow structure (see Fig. 5 of Olson et al. (1999) and Figs. 6-7 of Aubert et al., 2008b).

The distinction between equatorial B_ϕ vs. mid-latitude B_θ magnetic boundary layers (e.g. Fig. 2) reflects the competition between rotation and convection in the fluid dynamics. When rotation dominates buoyancy is outwards transported to the equator whereas as convection becomes stronger more buoyancy is transported towards high latitudes (e.g. Tilgner and Busse, 1997; Busse and Simitev, 2006, 2015; Yadav et al., 2016; Guervilly and Cardin, 2017; Miquel et al., 2018; Amit et al., 2020). We found that thinner/thicker magnetic boundary layers are more associated with B_θ/B_ϕ , respectively (Fig. 10). Stronger convection (and hence stronger induction) gives thinner layers (Fig. 6), more buoyancy transport to higher latitudes and magnetic boundary layers associated with B_θ (Fig. 10); Conversely, relatively weaker convection (and hence larger role of rotation) results in thicker layers (Fig. 6), more

equatorial buoyancy transport and layers associated with B_ϕ (Fig. 10). This relation between the horizontal field orientation vs. the competition between rotation and convection is further demonstrated when considering the limit between dynamical regimes. In Fig. 15 we plot ζ^{B_ϕ/B_θ} as a function of $E^{8/5}Ra$, which represents the limit between rapidly rotating and transitional regimes in spherical shells (Gastine et al., 2016; Long et al., 2020). Although there is clear evidence in Fig. 15 for dependence on Pm and q^* (see in particular the column of different ζ^{B_ϕ/B_θ} values for $E^{8/5}Ra = 7$), which could not be captured in the non-magnetic homogeneous boundary condition simulations of Gastine et al. (2016), the overall decreasing trend confirms that on approach to the rapidly rotating regime (smaller $E^{8/5}Ra$) the layers are governed by B_ϕ while further into the transitional regime more B_θ layers emerge. Interpolations to Earth's core conditions yield either a balance between B_ϕ and B_θ layers or more B_ϕ , suggesting that the flow in the core is either governed by rotation effects (e.g. Pais and Jault, 2008) or a more balanced dynamics of rotation and convection prevails. This distinction has important implications for core dynamics, in particular for the validity of the quasi-geostrophic approximation and the ensuing equatorial symmetry in the core flow. Unfortunately the vast range of interpolated ζ^{B_ϕ/B_θ} values (Fig. 10) hardly constrains this debate.

A key ingredient in dynamo models with heterogeneous boundary heat flux is the amplitude of the imposed lateral variation, which is quantified by q^* (11). In models with slightly superadiabatic mean convection at the outer boundary, the heat flux heterogeneity may lead to some regions with apparent local stratification (Olson et al., 2017, 2018; Mound et al., 2019; Mound and Davies 2020). In our dynamo models q^* does not exceed unity (Table 1), i.e. the outer boundary heat flux is superadiabatic throughout the top of the shell.

Evaluating q^* for Earth's core is not trivial. Nakagawa and Tackley (2008) estimated based on mantle convection simulations $q^* \sim 1.6$. More

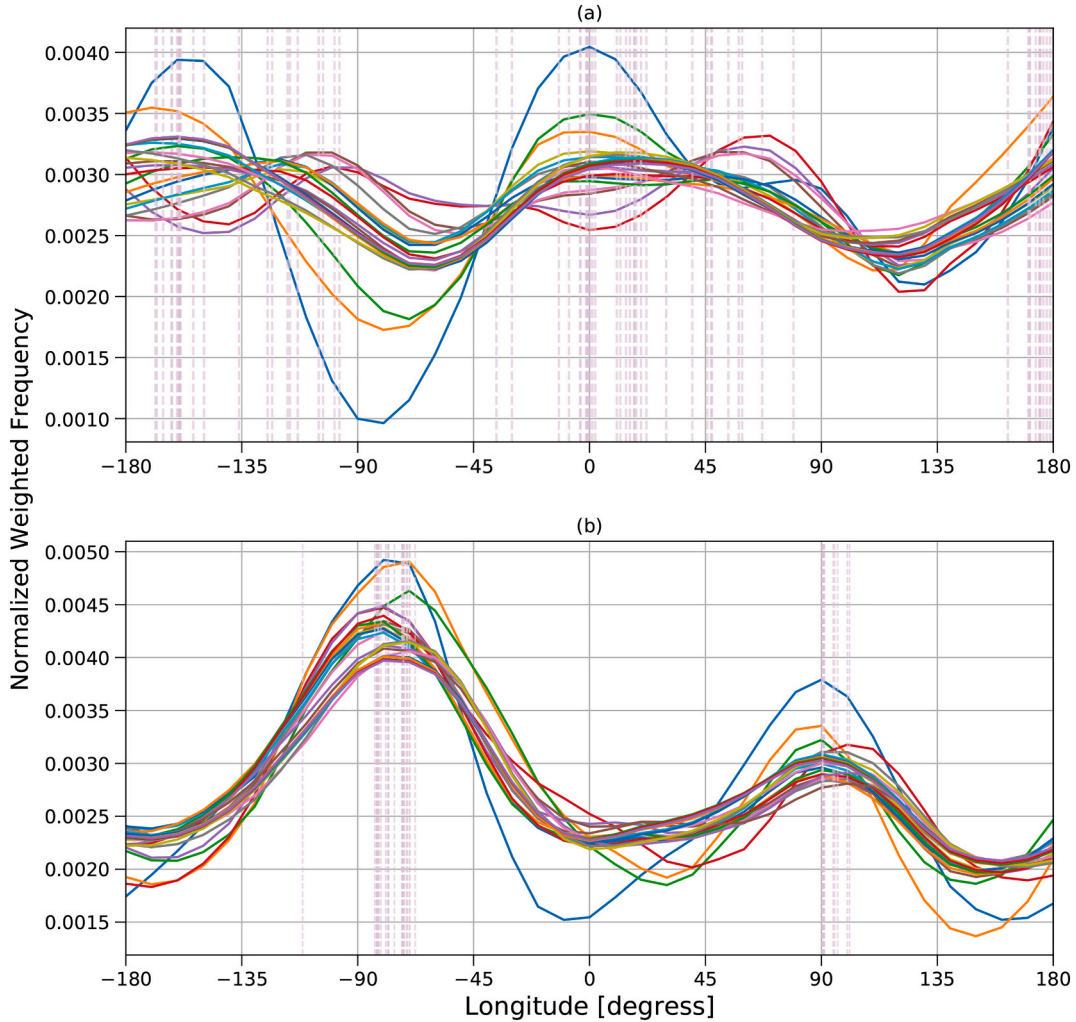


Fig. 13. Moving averages of magnetic boundary layers longitudinal histograms for B_ϕ (a) and B_θ (b) using the stack of all snapshots of each dynamo model with $f = 0.5$. Dashed vertical lines denote the peaks $\mathcal{P}_\phi^{B_\phi}$ (a) and $\mathcal{P}_\theta^{B_\theta}$ (b). Each colour represents a model.

realistic simulations that use plate tectonics reconstruction as an upper mechanical forcing obtain $q^* \sim 0.6$ (Rudolph and Zhong 2014; Zhong and Rudolph 2015; Olson et al., 2017). Proper consideration of only the superadiabatic part for the mean CMB heat flux q_0 in (11) led Mound et al. (2019) to infer a very large q^* . In contrast, if core convection is dominantly compositional, it is sensible to normalize q^* by the mean buoyancy flux rather than by q_0 , which may result in a very small q^* (Aubert et al., 2013). In our dynamo models the setup corresponds to thermochemical convection with the mean buoyancy flux represented by the mean CMB heat flux (Aubert et al., 2008a). In summary, the moderate q^* values in our dynamo models are of the same order as inferences from mantle convection simulations (Nakagawa and Tackley 2008; Rudolph and Zhong 2014; Zhong and Rudolph 2015; Olson et al., 2017) while avoiding violation of the Boussinesq approximation on which the models rely (Sahoo et al., 2016).

We find two preferred longitudes of magnetic boundary layers associated with each magnetic field horizontal component. For each component the two peaks are 180 degrees apart. In most models the B_ϕ and B_θ peaks are 90 degrees apart, though the former are more dispersed (Fig. 13). These results clearly indicate control of the dominant Y_2^2 in the tomographic model (Fig. 11a) on the longitudes of magnetic boundary layer. However, the B_ϕ and B_θ peaks correlate with low and high heat flux respectively, which is somewhat counter-intuitive and therefore deserves attention.

In the dynamo models of Aubert et al., 2008b with homogeneous

outer boundary heat flux the strongest upwellings/downwellings reside near the edge of the tangent cylinder. In our models, in addition, persistent mantle-driven upwellings/downwellings occur along longitudinal strips, as prescribed by the imposed heat flux pattern. In the models of Aubert et al., 2008b B_ϕ field lines are formed deep at the equatorial plane at longitudes of cyclones that correlate with outer boundary downwellings. From the deep equatorial plane B_ϕ is advected to the outer boundary by equatorial upwelling secondary flow (Aubert et al., 2008b). In contrast, in our models mantle-driven upwellings appear at longitudes of low outer boundary heat flux at all latitudes including the equator. Prominent zonal flow may advect B_ϕ at depth to other longitudes from where the mantle-driven upwellings carry it to the outer boundary. The different longitudes of peaks in Fig. 13a may reflect these two different effects.

The case of B_θ layers is different because this horizontal field component is produced close to the outer boundary (Aubert et al., 2008b). In addition we find little dispersion among our dynamo models with longitude peaks of B_θ around -90° and 90° (Fig. 13b). However, according to Aubert et al., 2008b B_θ is produced by anti-cyclones, hence it is expected to correlate with outer boundary heat flux minima at around 0° and 180° (Fig. 11a). This apparent discrepancy can be reconciled considering the large scale of the heat flux heterogeneity. Note that the field component parallel to the rotation axis B_z is aligned with the center of the anticyclone, whereas B_θ is stretched from the flow column to its margins (see Fig. 7 of Aubert et al., 2008b). This may

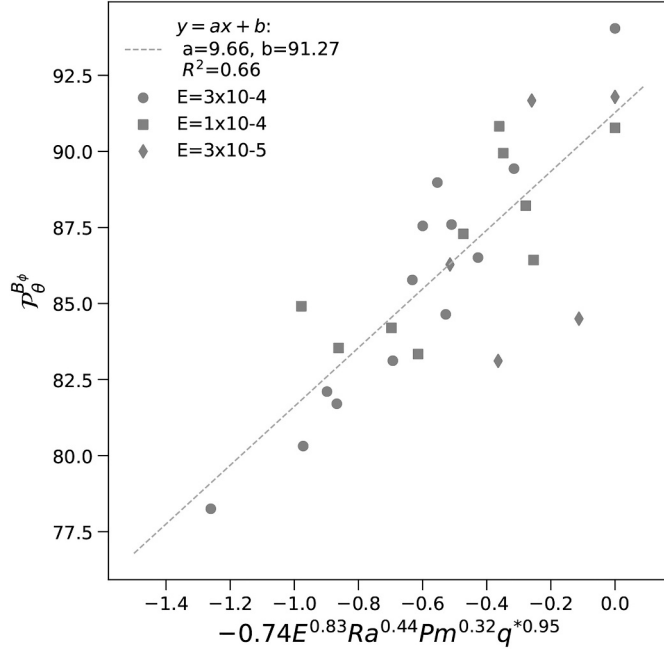


Fig. 14. Scaling law fit for the weighted co-latitude of the B_ϕ magnetic boundary layers $P_\theta^{B_\phi}$ vs. the dynamo control parameters. The goodness of fit is measured by R^2 . Dynamo models with different E values are denoted by different symbols (see legend).

Table 2

Fitting parameters for $\langle L_r \rangle$ and $\langle L_r^{pol} \rangle$ scaling laws.

x1	x2	x3	R^2
-0.242	-	-	0.818
-0.206	-0.039	-	0.874
-0.213	-	-0.029	0.836
y1	y2	y3	R^2
-0.217	-	-	0.815
-0.186	-0.046	-	0.900
-0.187	-	-0.044	0.861

The powers $x1$, $x2$, $x3$ and $y1$, $y2$, $y3$ correspond to the powers in $\langle L_r \rangle = ARm^{x1}E^{x2}Pm^{x3}$ and $\langle L_r^{pol} \rangle = B(Rm^{pol})^{y1}E^{y2}Pm^{y3}$ where A and B are pre-factors. The goodness of fits are measured by R^2 .

explain the persistent shift of the B_θ longitude peaks of our dynamo models from low heat flux longitudes.

In summary, we emphasize that the existence of two longitude peaks at each dynamo model and for each horizontal field component, the 180 degrees distance between the two peaks for each component, and the 90 degrees distance between B_ϕ and B_θ peaks in most models, all point to a clear mantle control on the persistent longitudes of magnetic boundary layers. These results suggest that below Africa and mid-Pacific the toroidal field is oriented in the east-west direction, whereas below the Americas and east Asia the toroidal field is oriented in the north-south direction.

The locations of magnetic boundary layers may be related to those of the geomagnetic surface intensity minima, the well known South Atlantic Anomaly. Reversed flux patches are formed from the expulsion of horizontal magnetic field (e.g. Bloxham, 1986; Troyano et al., 2020) and may yield low intensity field at Earth's surface (Olson and Amit, 2006; De Santis et al., 2013; Aubert, 2015; Tarduno et al., 2015; Pavón-Carrasco and De Santis, 2016; Terra-Nova et al., 2017). Aubert (2015) assimilated historical geomagnetic data with an Earth-like numerical dynamo model. He found an eccentric anticyclonic gyre below the South Atlantic, in agreement with core flow models inverted from the geomagnetic secular variation (Pais and Jault, 2008; Gillet et al., 2009,

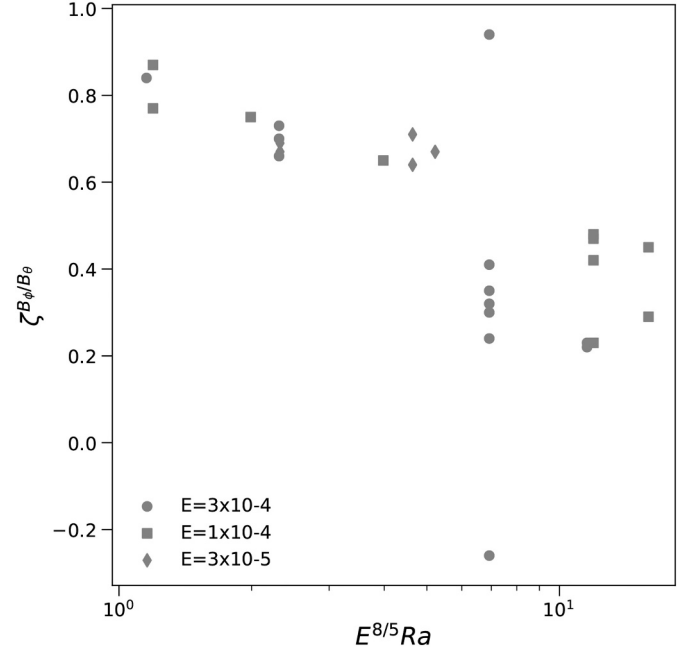


Fig. 15. The parameter defining horizontal field orientation within a magnetic boundary layer ζ^{B_ϕ/B_θ} (16) vs. $E^{8/5}Ra$ which represents the limit between the rapidly rotating and transitional regimes (Gastine et al., 2016). Dynamo models with different E values are denoted by different symbols (see legend).

2015a). In his model the South Atlantic Anomaly drifts westward from its present location below mainland Brazil to mid Pacific within a few decades. Terra-Nova et al. (2019) used numerical dynamo models with heterogeneous outer boundary heat flux to investigate mantle control on the position of intensity minima at Earth's surface. They found a persistent large-scale upwelling structure in the South Atlantic with recurrent minima in its borders below South America and the Indian Ocean. In this study, close to these locations we find peaks of B_θ layers. We speculate that the persistence of surface field minima at South America may imply a location of magnetic flux expulsion of B_θ field lines below the CMB prescribed by lowermost mantle heterogeneities.

Our estimates for the magnetic boundary layer thickness below the CMB have interesting implications for the effective magnetic diffusion time and the effective magnetic Reynolds number of Earth's core. From hereafter we refer to these two quantities as 'local' (rather than 'effective') to emphasize their sporadic nature (Fig. 2). The magnetic diffusion time is defined by

$$\tau_\eta = \frac{D^2}{\eta} \quad (19)$$

The magnetic advection time is defined by

$$\tau_u = \frac{D}{U} \quad (20)$$

The magnetic Reynolds number is

$$Rm \equiv \frac{\tau_\eta}{\tau_u} \quad (21)$$

If the same length-scale D is used for both time scales the classical definition of Rm (1) is recovered. Substituting outer core shell thickness $D = 2265$ km and classical values $U = 5 \times 10^{-4}$ m/s and $\eta = 1$ m²/s, (20) and (19) give $\tau_u \approx 140$ yr and $\tau_\eta \approx 160$ kyr, respectively. The local magnetic diffusion time is derived by substituting the appropriate radial length scale L_r into (19):

$$\tau_\eta^{loc} = \frac{L_r^2}{\eta} = \tau_\eta \left(\frac{L_r}{D} \right)^2 \quad (22)$$

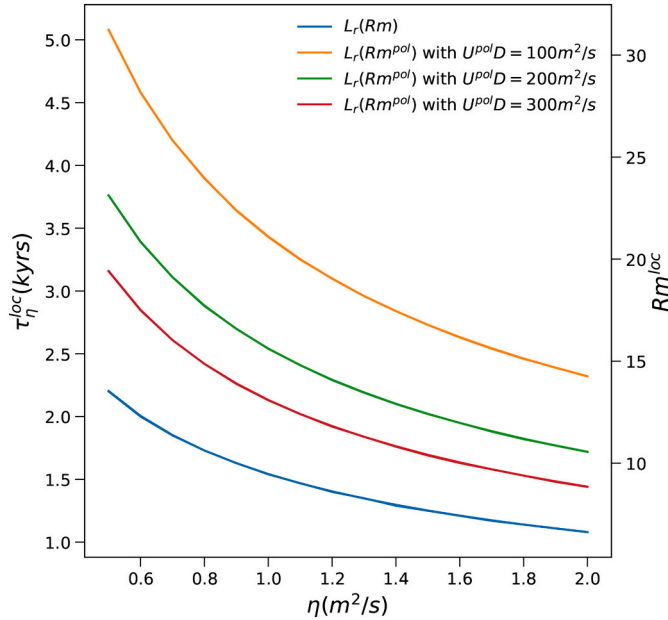


Fig. 16. Local magnetic diffusion time τ_{η}^{loc} (22) and local magnetic Reynolds number Rm^{loc} (23) vs. magnetic diffusivity η . For the blue curve we set $UD = 1000 \text{ m}^2/\text{s}$ and we apply the scaling law of $\langle L_r \rangle$ vs. Rm (Fig. 6 left). For the other curves a range of $U^{pol}D = 100 - 300 \text{ m}^2/\text{s}$ (Amit and Olson 2004; Huguet et al., 2018) is explored and we apply the scaling law of $\langle L_r \rangle$ vs. Rm^{pol} (Fig. 6 right). (For interpretation of the references to colour in this figure legend, the reader is referred to the web version of this article.)

Then a local magnetic Reynolds number is defined by

$$Rm^{loc} = \frac{\tau_{\eta}^{loc}}{\tau_u} = \frac{UL_r^2}{\eta D} = Rm \left(\frac{L_r}{D} \right)^2 \quad (23)$$

For the same values of D , U and η substituting our range of $L_r \approx 220\text{--}330 \text{ km}$ (Fig. 6) into (22) and (23) gives $\tau_{\eta}^{loc} \approx 1.5\text{--}3.4 \text{ kyr}$ and $Rm^{loc} \approx 10\text{--}20$. These values correspond to local magnetic diffusion time two orders of magnitude shorter than the classical τ_{η} value, and consequently local magnetic Reynolds number two orders of magnitude smaller than the classical Rm . Our results therefore imply a significantly larger role of diffusion in core dynamics, in agreement with previous assessments (Amit and Christensen, 2008; Chulliat and Olsen, 2010; Finlay et al., 2016; Barrois et al., 2017, 2018; Gillet et al., 2019). However, our $Rm^{loc} > 1$ values still suggest that induction effects dominate over diffusive, in contrast to the model of Metman et al. (2019) where diffusion accounts for the entire SV.

So far we used fixed values for D , U and η , although the latter is under debate (e.g. Pozzo et al., 2012; Konôpková et al., 2016; Ohta et al., 2016; Driscoll and Du 2019). The local magnetic diffusion time and the local magnetic Reynolds number both depend in a non-trivial way on the magnetic diffusivity. While η appears in the denominators of (22) and (23), it also appears in the estimates of the magnetic Reynolds numbers of Earth's core that we use to infer $\langle L_r \rangle$ (see Fig. 6). In Fig. 16 we use the diagnostics of $\langle L_r \rangle$ while considering η a free parameter. For all cases we set $UD = 1000 \text{ m}^2/\text{s}$. In the blue curve we set $\langle L_r \rangle$ from the Rm extrapolation. In the other three curves we consistently set $U^{pol}D = 100, 200, 300 \text{ m}^2/\text{s}$ and $\langle L_r \rangle$ from the Rm^{pol} interpolations. Fig. 16 demonstrates that larger η results in smaller τ_{η}^{loc} and Rm^{loc} , but the decrease is slower than inverse to η because larger η corresponds to thicker layers (Fig. 6). We find $\tau_{\eta}^{loc} \approx 1.1\text{--}2.2 \text{ kyr}$ based on the total core flow estimate and $1.4\text{--}5.1 \text{ kyr}$ based on the poloidal core flow estimate. These results correspond to $Rm^{loc} \approx 6.7 - 13.5$ and $8.9 - 31.2$ respectively (Fig. 16). In summary, even when some uncertainties in the magnetic diffusivity and in the poloidal flow magnitude are taken into account, the local magnetic diffusion time is merely

a few kyrs and the local magnetic Reynolds number corresponds to diffusive SV being only an order of magnitude smaller than induction. These low values merit re-evaluation of the induction processes at depth within Earth's core.

Declaration of Competing Interest

None.

Acknowledgments

We are grateful to Dominique Jault and two anonymous reviewers for constructive reviews that improved the paper. This work was supported by the Programme National de Planétologie (PNP) of CNRS/INSU, co-funded by CNES. F. T-N. acknowledges São Paulo Research Foundation (FAPESP) for grant 2018/07410-3.

References

- Alboussière, T., Lingwood, R.J., 2000. A model for the turbulent hartmann layer. *Phys. Fluids* 12 (6), 1535–1543.
- Amit, H., 2014. Can downwelling at the top of the Earth's core be detected in the geomagnetic secular variation? *Phys. Earth Planet. Inter.* 229, 110–121.
- Amit, H., Choblet, G., 2009. Mantle-driven geodynamo features - effects of post-Perovskite phase transition. *Earth Planets Space* 61, 1255–1268.
- Amit, H., Choblet, G., 2012. Mantle-driven geodynamo features - effects of compositional and narrow D" anomalies. *Earth Planet. Inter.* 190–191, 34–43.
- Amit, H., Choblet, G., Tobie, G., Terra-Nova, F., Čadež, O., Bouffard, M., 2020. Cooling patterns in rotating thin spherical shells – application to Titan's subsurface ocean. *Icarus* 338, 113509.
- Amit, H., Christensen, U.R., 2008. Accounting for magnetic diffusion in core flow inversions from geomagnetic secular variation. *Geophys. J. Int.* 175, 913–924.
- Amit, H., Deschamps, F., Choblet, G., 2015. Numerical dynamos with outer boundary heat flux inferred from probabilistic topography—consequences for latitudinal distribution of magnetic flux. *Geophys. J. Int.* 203, 840–855.
- Amit, H., Olson, P., 2004. Helical core flow from geomagnetic secular variation. *Phys. Earth Planet. Inter.* 147, 1–25.
- Aubert, J., 2013. Flow throughout the Earth's core inverted from geomagnetic observations and numerical dynamo models. *Geophys. J. Int.* 192, 537–556.
- Aubert, J., 2015. Geomagnetic forecasts driven by thermal wind dynamics in the Earth's core. *Geophys. J. Int.* 203, 1738–1751.
- Aubert, J., Amit, H., Hulot, G., 2007. Detecting thermal boundary control in surface flows from numerical dynamos. *Phys. Earth Planet. Inter.* 160, 143–156.
- Aubert, J., Amit, H., Hulot, G., Olson, P., 2008a. Thermo-chemical wind flows couple Earth's inner core growth to mantle heterogeneity. *Nature* 454, 758–761.
- Aubert, J., Aurnou, J., Wicht, J., 2008b. The magnetic structure of convection-driven numerical dynamos. *Geophys. J. Int.* 172, 945–956.
- Aubert, J., Finlay, C.C., Fournier, F., 2013. Bottom-up control of geomagnetic secular variation by the Earth's inner core. *Nature* 502, 219–223.
- Aubert, J., Gastine, T., Fournier, A., 2017. Spherical convective dynamos in the rapidly rotating asymptotic regime. *J. Fluid Mech.* 813, 558–593.
- Aubert, J., Labrosse, S., Poitou, C., 2009. Modelling the paleo-evolution of the geodynamo. *Geophys. J. Int.* 179, 1414–1428.
- Aurnou, J., Andreadis, S., Zhu, L., Olson, P., 2003. Experiments on convection in Earth's core tangent cylinder. *Earth Planet. Sci. Lett.* 212, 119–134.
- Backus, G.E., 1968. Kinematics of geomagnetic secular variation in a perfectly conducting core. *Philos. Trans. R. Soc. Lond.* A263, 239–266.
- Barrois, O., Gillet, N., Aubert, J., 2017. Contributions to the geomagnetic secular variation from a reanalysis of core surface dynamics. *Geophys. J. Int.* 211 (1), 50–68.
- Barrois, O., Gillet, N., Aubert, J., Barrois, O., Hammer, M.D., Finlay, C.C., Martin, Y., Gillet, N., 2018. Erratum: 'Contributions to the geomagnetic secular variation from a reanalysis of core surface dynamics' and 'Assimilation of ground and satellite magnetic measurements: inference of core surface magnetic and velocity field changes'. *Geophys. J. Int.* 216 (3), 2106–2113.
- Beggan, C., Whaler, K., 2008. Core flow modelling assumptions. *Phys. Earth Planet. Inter.* 167, 217–222.
- Ben-Yosef, E., Tauxe, L., Levy, T.E., Shaar, R., Ron, H., Najjar, M., 2009. Geomagnetic intensity spike recorded in high resolution slag deposit in Southern Jordan. *Earth Planet. Sci. Lett.* 287 (3–4), 529–539.
- Bloxham, J., 1986. The expulsion of magnetic flux from the Earth's core. *Geophys. J. R. astr. Soc.* 87, 669–678.
- Bloxham, J., Gubbins, D., 1985. The secular variation of the Earth's magnetic field. *Nature* 325, 511–513.
- Bloxham, J., Gubbins, D., 1986. Geomagnetic field analysis-IV. Testing the frozen-flux hypothesis. *Geophys. J. Int.* 84 (1), 139–152.
- Buffett, B., 2014. Geomagnetic fluctuations reveal stable stratification at the top of the Earth's core. *Nature* 507, 484–487.
- Buffett, B., Knežek, N., Holme, R., 2016. Evidence for MAC waves at the top of Earth's core and implications for variations in length of day. *Geophys. J. Int.* 204 (3), 1789–1800.

- Busse, F.H., Simitev, R.D., 2006. Parameter dependences of convection-driven dynamos in rotating spherical fluid shells. *Geophys. Astrophys. Fluid Dyn.* 100 (4–5), 341–361.
- Busse, F., Simitev, R., 2015. Planetary dynamos. In: Schubert, G. (Ed.), *Treatise on Geophysics* (Second Edition). Vol. 10. Elsevier.
- Chulliat, A., Hulot, G., 2001. Geomagnetic secular variation generated by a tangentially geostrophic flow under the frozen-flux assumption—I. necessary conditions. *Geophys. J. Int.* 147 (2), 237–246.
- Chulliat, A., Olsen, N., 2010. Observation of magnetic diffusion in the Earth's outer core from Magsat, Orsted and CHAMP data. *J. Geophys. Res.* 115, B05105.
- Davies, C.J., Gubbins, D., Jimack, P.K., 2009. Convection in a rapidly rotating spherical shell with an imposed laterally varying thermal boundary condition. *J. Fluid Mech.* 641 (335–358), 15.
- Davies, C.J., Gubbins, D., Willis, A., Jimack, P.K., 2008. Time-averaged paleomagnetic field and secular variation: predictions from dynamo solutions based on lower mantle seismic tomography. *Phys. Earth Planet. Inter.* 169, 194–203.
- De Santis, A., Qamili, E., Wu, L., 2013. Toward a possible next geomagnetic transition? *Nat. Hazards Earth Syst. Sci.* 13, 3395–3403.
- Driscoll, P.E., Du, Z., 2019. Geodynamo conductivity limits. *Geophys. Res. Lett.* 46 (14), 7982–7989.
- Dziewonski, A.M., Anderson, D.L., 1981. Preliminary reference earth model. *Phys. Earth Planet. Inter.* 25 (4), 297–356.
- Finlay, C.C., 2008. Historical variation of the geomagnetic axial dipole. *Phys. Earth Planet. Inter.* 170, 1–14.
- Finlay, C.C., Amit, H., 2011. On flow magnitude and field-flow alignment at Earth's core surface. *Geophys. J. Int.* 186, 175–192.
- Finlay, C.C., Aubert, J., Gillet, N., 2016. Gyre-driven decay of the Earth's magnetic dipole. *Nat. Commun.* 7, 10422. <https://doi.org/10.1038/ncomms10422>.
- Gastine, T., Wicht, J., Aubert, J., 2016. Scaling regimes in spherical shell rotating convection. *J. Fluid Mech.* 808, 690–732.
- Gillet, N., Barrois, O., Finlay, C.C., 2015a. Stochastic modelling of the Earth's magnetic field: inversion for covariances over the observatory era. *Earth Planets Space* 67, 67–71.
- Gillet, N., Huder, L., Aubert, J., 2019. A reduced stochastic model of core surface dynamics based on geodynamo simulations. *Geophys. J. Int.* 219 (1) (552–539).
- Gillet, N., Jault, D., Finlay, C., 2015b. Planetary gyre, time-dependent eddies, torsional waves, and equatorial jets at the Earth's core surface. *J. Geophys. Res.* 120 (6), 3991–4013.
- Gillet, N., Jault, D., Finlay, C., Olsen, N., 2013. Stochastic modeling of the Earth's magnetic field: inversion for covariances over the observatory era. *Geochem. Geophys. Geosyst.* 14 (4), 766–786.
- Gillet, N., Pais, M.A., Jault, D., 2009. Ensemble inversion of time-dependent core flow models. *Geochem. Geophys. Geosyst.* 10, Q06004.
- Gubbins, D., 1987. Mechanism for geomagnetic polarity reversals. *Nature* 326, 167–169.
- Gubbins, D., 2003. Thermal core-mantle interactions: Theory and observations. In: Dehant, V., Creager, K., Karato, S., Zatman, S. (Eds.), *Earth's Core: Dynamics, Structure and Rotation*. AGU Geodynamics Series - American Geophysical Union.
- Gubbins, D., Sreenivasan, B., Mound, J., Rost, S., 2011. Melting of the Earth's inner core. *Nature* 473, 361–363.
- Gubbins, D., Willis, A.P., Sreenivasan, B., 2007. Correlation of Earth's magnetic field with lower mantle thermal and seismic structure. *Phys. Earth Planet. Inter.* 162, 256–260.
- Guervilly, C., Cardin, P., 2017. Multiple zonal jets and convective heat transport barriers in a quasi-geostrophic model of planetary cores. *Geophys. J. Int.* 211 (1), 455–471.
- Holme, R., 2015. Large-scale flow in the core. In: Schubert, G. (Ed.), *Treatise on Geophysics* (Second Edition). vol. 8 Elsevier.
- Huguet, L., Amit, H., Alboussière, T., 2018. Geomagnetic dipole changes and upwelling/downwelling at the top of the Earth's core. *Front. Earth Sci.* 6, 170.
- King, E.M., Stellmach, S., Noir, J., Hansen, U., Aurnou, J.M., 2009. Boundary layer control of rotating convection systems. *Nature* 457, 301–304.
- Konôpková, Z., McWilliams, R., Gómez-Pérez, N., Goncharov, A.F., 2016. Direct measurement of thermal conductivity in solid iron at planetary core conditions. *Nature* 534, 99–101.
- Lesur, V., Whaler, K., Wardinski, I., 2015. Are geomagnetic data consistent with stably stratified flow at the core–mantle boundary? *Geophys. J. Int.* 201 (2), 929–946.
- Lloyd, D., Gubbins, D., 1990. Toroidal fluid motion at the top of the Earth's core. *Geophys. J. Int.* 100 (3), 455–467.
- Long, R.S., Mound, J.R., Davies, C.J., Tobias, S.M., 2020. Scaling behaviour in spherical shell rotating convection with fixed-flux thermal boundary conditions. *J. Fluid Mech.* 889, 690–732.
- Masters, G., Laske, G., Bolton, H., Dziewonski, A., Karato, S., Forte, A., Liebermann, R., Masters, G., Stixrude, L., 2000. The relative behavior of shear velocity, bulk sound velocity, and compressional velocity in the mantle: implications for chemical and thermal structure. In: *Earth's Deep Interior: Mineral Physics and Tomography From the Atomic to the Global Scale*. vol. 117 AGU monograph, Washington D.C.
- Metman, M.C., Livermore, P.W., Mound, J.E., 2018. The reversed and normal flux contributions to axial dipole decay for 1880–2015. *Phys. Earth Planet. Inter.* 276, 106–117.
- Metman, M.C., Livermore, P.W., Mound, J.E., Beggan, C.D., 2019. Modelling decadal secular variation with only magnetic diffusion. *Geophys. J. Int.* 219 (S1), S58–S82.
- Miquel, B., Xie, J., Featherstone, N., Julien, K., Knobloch, E., 2018. Equatorially trapped convection in a rapidly rotating shallow shell. *Phys. Rev. Fluids* 3 (5), 053801.
- Moffatt, H., 1978. *Magnetic Field Generation in Electrically Conducting Fluids*. Cambridge University Press, Cambridge, U.K.
- Mound, J.E., Davies, C.J., 2020. Scaling laws for regional stratification at the top of Earth's core. *Geophys. Res. Lett.* 47 (e2020GL087715).
- Mound, J., Davies, C., Rost, S., Aurnou, J., 2019. Regional stratification at the top of Earth's core due to core–mantle boundary heat flux variations. *Nat. Geosci.* 12, 575–580.
- Nakagawa, T., Tackley, P.J., 2008. Lateral variations in cmb heat flux and deep mantle seismic velocity caused by a thermal-chemical-phase boundary layer in 3d spherical convection. *Earth Planet. Sci. Lett.* 271, 348–358.
- Ohta, K., Kuwayama, Y., Hirose, K., Shimizu, K., Ohishi, Y., 2016. Experimental determination of the electrical resistivity of iron at Earth's core conditions. *Nature* 534, 95–98.
- Olson, P., Amit, H., 2006. Changes in earth's dipole. *Naturwissenschaften* 93, 519–542.
- Olson, P., Christensen, U.R., 2002. The time averaged magnetic field in numerical dynamos with nonuniform boundary heat flow. *Geophys. J. Int.* 151, 809–823.
- Olson, P., Christensen, U.R., Glatzmaier, G.A., 1999. Numerical modeling of the geodynamo: mechanisms of field generation and equilibration. *J. Geophys. Res.* 104, 10383–110404.
- Olson, P., Landeau, M., Reynolds, E., 2017. Dynamo tests for stratification below the core-mantle boundary. *Phys. Earth Planet. Inter.* 271, 1–18.
- Olson, P., Landeau, M., Reynolds, E., 2018. Outer core stratification from the high latitude structure of the geomagnetic field. *Front. Earth Sci.* 6, 140.
- Pais, M.A., Jault, D., 2008. Quasi-geostrophic flows responsible for the secular variation of the Earth's magnetic field. *Geophys. J. Int.* 173, 421–443.
- Pavón-Carrasco, F.J., De Santis, A., 2016. The South Atlantic anomaly: the key for a possible geomagnetic reversal. *Front. Earth Sci.* 4, 40.
- Pedlosky, J., 1987. *Geophysical Fluid Dynamics*. Springer-Verlag, New York, USA.
- Poletti, W., Biggin, A., Trindade, R.I.F., Hartmann, G.A., Terra-Nova, F., 2018. Continuous millennial decrease of the Earth's magnetic axial dipole. *Phys. Earth Planet. Inter.* 274, 72–86.
- Pozzo, M., Davies, C., Gubbins, D., Alfe, D., 2012. Thermal and electrical conductivity of iron at Earth's core conditions. *Nature* 485, 355–358.
- Roberts, P.H., Scott, S., 1965. On analysis of the secular variation, 1, a hydromagnetic constraint: theory. *J. Geomagn. Geoelectr.* 17, 137–151.
- Rudolph, M.L., Zhong, S.J., 2014. History and dynamics of net rotation of the mantle and lithosphere. *Geochem. Geophys. Geosyst.* 15, 3645–3657.
- Sahoo, S., Sreenivasan, B., Amit, H., 2016. Dynamos driven by weak thermal convection and heterogeneous outer boundary heat flux. *Phys. Earth Planet. Inter.* 250, 35–45.
- Schaeffer, N., 2013. Efficient spherical harmonic transforms aimed at pseudospectral numerical simulations. *Geochem. Geophys. Geosyst.* 14 (3), 751–758.
- Schubert, G., Turcotte, D., Olson, P., 2001. *Mantle Convection in the Earth and Planets*. Cambridge University Press.
- Shaar, R., Ben-Yosef, E., Tauxe, L., Ron, H., Ebert, Y., Zuckerman, S., Finkelstein, I., Agnon, A., 2011. Geomagnetic field intensity: how high can it get? How fast can it change? Constraints from Iron Age copper slag. *Earth Planet. Sci. Lett.* 301, 297–306.
- Shaar, R., Tauxe, L., Ron, H., Ebert, Y., Zuckerman, S., Finkelstein, I., Agnon, A., 2016. Large geomagnetic field anomalies revealed in bronze to iron age archeomagnetic data from Tel Megiddo and Tel Hazor, Israel. *Earth Planet. Sci. Lett.* 442, 173–185.
- Takahashi, F., Tsunakawa, H., Matsushima, M., Mochizuki, N., Honkura, Y., 2008. Effects of thermally heterogeneous structure in the lowermost mantle on the geomagnetic field strength. *Earth Planet. Sci. Lett.* 272 (3–4), 738–746.
- Tarduno, J.A., Watkeys, M.K., Huffman, T.N., Cottrell, D.C., Blackman, E.G., Wendt, A., Scribner, A.C., Wagner, C.L., 2015. Antiquity of the south Atlantic anomaly and evidence for top-down control on the geodynamo. *Nat. Commun.* 6, 7865. <https://doi.org/10.1038/ncomms8865>.
- Terra-Nova, F., Amit, H., Choblet, G., 2019. Preferred locations of weak surface field in numerical dynamos with heterogeneous core-mantle boundary heat flux: consequences for the South Atlantic anomaly. *Geophys. J. Int.* 217 (2), 1179–1199.
- Terra-Nova, F., Amit, H., Hartmann, G.A., Trindade, R.I.F., 2015. The time dependence of reversed archeomagnetic flux patches. *J. Geophys. Res.* 120 (2), 691–704.
- Terra-Nova, F., Amit, H., Hartmann, G.A., Trindade, R.I.F., 2016. Using archaeomagnetic field models to constrain the physics of the core: robustness and preferred locations of reversed flux patches. *Geophys. J. Int.* 206 (3), 1890–1913.
- Terra-Nova, F., Amit, H., Hartmann, G.A., Trindade, R.I.F., Pinheiro, K.J., 2017. Relating the South Atlantic anomaly and geomagnetic flux patches. *Phys. Earth Planet. Inter.* 266, 39–53.
- Tilgner, A., Busse, F.H., 1997. Finite-amplitude convection in rotating spherical fluid shells. *J. Fluid Mech.* 332, 359–376.
- Troyano, M., Fournier, A., Gallet, Y., Finlay, C., 2020. Imprint of magnetic flux expulsion at the core–mantle boundary on geomagnetic field intensity variations. *Geophys. J. Int.* 221 (3), 1984–2009.
- Whaler, K., 1980. Does the whole of Earth's core convect? *Nature* 287, 528–530.
- Whaler, K., 1986. Geomagnetic evidence for fluid upwelling at the core-mantle boundary. *Geophys. J. R. Astr. Soc.* 86, 563–588.
- Whaler, K., Holme, R., 2007. Consistency between the flow at the top of the core and the frozen-flux approximation. *Earth Planets Space* 59, 1219–1229.
- Wicht, J., 2002. Inner-core conductivity in numerical dynamo simulations. *Phys. Earth Planet. Inter.* 132, 281–302.
- Yadav, R.K., Christensen, U.R., Wolk, S.J., Poppenhaeger, K., 2016. Magnetic Cycles in a Dynamo Simulation of Fully Convective M-Star Proxima Centauri. 833 (2), pp. L28.
- Zhong, S.J., Rudolph, M.L., 2015. On the temporal evolution of long-wavelength mantle structure of the Earth since the early Paleozoic. *Geochem. Geophys. Geosyst.* 16, 1599–1615.